Integrated flux and pool size analysis in plant central metabolism reveals unique roles of glycine and serine during photorespiration

Authors: Xinyu Fu[1], Luke M. Gregory[1,2], Sean E. Weise[1], Berkley J. Walker[1,2]*

[1] Michigan State University-Department of Energy Plant Research Laboratory, Michigan State University, East Lansing, MI 48824, USA

[2] Department of Plant Biology, Michigan State University, East Lansing, MI 48824, USA

*Correspondence to: Berkley Walker, berkley@msu.edu

Abstract

Photorespiration is an essential process juxtaposed between plant carbon and nitrogen metabolism that responds to dynamic environments. Photorespiration recycles inhibitory intermediates arising from oxygenation reactions catalyzed by rubisco back into the C_3 cycle, but it is unclear what proportions of its nitrogen-containing intermediates (glycine and serine) are exported into other metabolisms *in vivo* and how these pool sizes affect net CO_2 gas exchange during photorespiratory transients. To address this uncertainty, we measured rates of amino acid export from photorespiration using isotopically nonstationary metabolic flux analysis. This analysis revealed that ~23-41% of the photorespiratory carbon was exported from the pathway as serine under various photorespiratory conditions. Furthermore, we determined that the build-up and relaxation of glycine pools constrained a large portion of photosynthetic acclimation during photorespiratory transients. These results reveal the unique and important roles of glycine and serine in successfully maintaining various photorespiratory fluxes that occur under environmental fluctuations in nature and providing carbon and nitrogen for metabolism.

Main

In C_3 plants, photorespiration is a high-flux metabolic pathway that recycles the inhibitory 2-phosphoglycolate (2PG) produced from the oxygenation reaction catalyzed by ribulose-1,5-bisphosphate carboxylase-oxygenase (rubisco). The recycling of 2PG to the C_3 intermediate, 3-phosphoglycerate (3PGA) involves a series of energy-consuming reactions across multiple organelles [1,2]. Upon cursory consideration, photorespiration is often viewed as a wasteful process, because the conversion from glycine to serine releases a large amount of CO_2 and ammonia, the former is released from photorespiration and the latter is re-assimilated with high-energy cost. However, besides the beneficial removal of 2PG, photorespiration also plays a vital role in central metabolism due to its close interaction with many other pathways, especially nitrate assimilation [3–6]. Although the interaction between photorespiration and nitrate assimilation is not mechanistically clear, nitrate assimilation depends to some degree on photorespiration [5,7]. For example, plants grown under elevated CO_2 partial pressures with decreased photorespiration have decreased nitrate assimilation into organic nitrogen (N) compounds and total N concentration of plant tissues [8,9]. Additionally, the major route of ammonia assimilation, glutamate synthesis, increases as photorespiration increases possibly not only facilitating increased rates of ammonia recapture from photorespiration but also increased rates of *de novo* nitrate assimilation [10,11].

The mechanism linking photorespiration to nitrate assimilation could be related to the export of N-rich amino acids from photorespiration. Due to the high metabolic flux channeled through photorespiration, even small changes in photorespiratory flux could affect the flux distribution through central carbon (C) and N metabolism. The extent to which photorespiration operates as a closed cycle to regenerate 3-PGA for the C_3 cycle or as an open cycle allowing metabolite export to interacting metabolisms remains unknown [12]. Exporting glycine and serine from photorespiration into non-photorespiratory metabolism (*e.g.,* protein synthesis, providing amino groups to alternative metabolic processes or transport) instead of returning their C to the chloroplast as 3PGA additionally affects the CO_2 loss and the energy costs associated with recycling of 2PG into 3PGA.

Evidence for a fraction of photorespiratory C exported from photorespiration as glycine and/or serine is revealed in biochemical modeling of leaf photosynthesis [13]. The export of photorespiratory C as amino acids can explain the decreased rates of net CO_2 assimilation (A) in response to CO_2 and O_2 at high CO_2 partial pressures, typically 2-4 times ambient conditions and saturating illumination [13]. In this paper we define glycine and serine export as amino acids that leave photorespiratory metabolism, this includes amino acids that leave the leaf entirely, as in phloem exudate, but also to amino acids that leave photorespiration to participate in non-photorespiratory metabolism in the same leaf tissue. The fraction of photorespiratory C exported as amino acids estimated using photosynthetic models ranges between 0.3-

0.77 under the high CO_2 partial pressures where this approach can be used, with serine being the primary amino acid exported [14,15]. Exporting glycine and serine from photorespiration increases photosynthesis at high CO_2 partial pressures when carbon assimilation is limited by the availability of inorganic phosphate in the chloroplast [16].

Exporting glycine and serine from photorespiration is also coupled to the N flux to these amino acids. Specifically, this N flux out of photorespiration in the form of amino acids must be supplemented by increasing the *de novo* assimilation of N to replace the amino groups required for glyoxylate amination to glycine, potentially explaining why the estimated fraction of amino acid export increases with increasing NO_3^- availability [15]. Despite this compelling evidence for serine and glycine export under high CO_2 partial pressures when photorespiration is limited, it is unclear if high rates of amino acid export happen under more physiologically relevant CO_2 partial pressures and forms a regular component of central metabolism under more typical growing conditions. C export from photorespiration also raises interesting questions concerning the functional importance of photorespiration, since this export would not replenish C lost from the C_3 cycle following rubisco oxygenation.

Another uncertainty of photorespiration is the speed of its metabolic response and subsequent impact on *A*. Photorespiration is a dynamic process, responding to *A*, stomatal conductance, and light regimes. However, it is mostly investigated under steady-state conditions by comparing the metabolomic profile and physiology following different environmental and genetic perturbations [17–19]. Under non-steady-state conditions, amounts of photorespiratory intermediates are sensitive to photorespiratory conditions both in the long- and short-term [17–19]. Photorespiratory intermediates additionally accumulate during transient changes in rubisco oxygenation rate or when downstream photorespiratory reactions are not stoichiometrically balanced [20–24]. When photorespiratory intermediates upstream of the glycine decarboxylase (GDC) reaction like glycine accumulate, the CO_2 release per rubisco oxygenation should decrease proportionally, increasing subsequent *A* during this accumulation. Despite this theoretical underpinning, it is not clear if the change in glycine pools is large enough to affect *A* to a measurable degree during transients in photorespiratory rates.

The use of isotopic tracers and metabolic flux analysis (MFA) are powerful tools to resolve how metabolism responds to environmental changes [25,26]. For example, isotopic labeling with $^{13}CO_2$ in combination with varied CO_2 and/or O_2 mole fraction has been commonly used to infer the impact of photorespiration on leaf C metabolism. Under different CO_2/O_2 conditions, distinct ^{13}C labeling enrichment has been observed in many primary and specialized metabolites [20,27], as well as proteins [28,29]. These studies were usually performed at isotopic pseudo-steady state with a single time-point, which does not allow flux quantification in autotrophic metabolism [30]. Recent development of isotopically

nonstationary metabolic flux analysis (INST-MFA) more fully leverages the benefits of $^{13}CO_2$ labeling to provide a global assessment of C fluxes through autotrophic leaf metabolism [26,31–34]. INST-MFA is therefore a promising approach for estimating fluxes and metabolic responses to changes in photorespiratory rates *in vivo*.

Here, INST-MFA was applied to examine the C fluxes through and out of the photorespiratory pathway under different photorespiratory conditions manipulated by the O_2 mole fraction. This INST-MFA analysis gave a quantitative estimate of serine and glycine exported from photorespiration under steady-state conditions at ambient CO_2 partial pressures, which agreed with estimates made under high CO_2 partial pressures using estimates from CO_2 response curves. Metabolite pool size measurements of 38 central metabolites showed that glycine had the strongest changes in response to photorespiratory shifts. We also determined that changes in glycine concentration were large enough to explain 20-30% of the gain in net CO_2 assimilation when transitioning from low to high photorespiratory conditions.

Results

Isotopically Nonstationary Metabolic Flux Analysis

To estimate C flux distribution on central metabolism, transient ^{13}C labeling experiments were performed on fully expanded *Nicotiana tabacum* (tobacco) leaves after short-term acclimation to three O_2 conditions (2%, 21%, and 40%). The labeling experiments were carried out at the same irradiance as the growth chamber (100 μmol m^{-2} s^{-1}) to minimize changes in metabolism due to light acclimation. Metabolic fluxes through central metabolism were determined from a metabolic network model (Supplementary Data 1), mass isotopologue distributions (MIDs) during the transient labeling period (Supplementary Data 2), and measured input and output fluxes to constrain the flux solutions. The independently determined input and output fluxes used to constrain the flux solution included the A, rubisco oxygenation rate (v_o), rubisco carboxylation rate (v_c), starch and sucrose production rates, and output flux ratios of amino acids and sucrose measured in vascular exudate (Supplementary Table 1 and 2 and Supplementary Method 1-4). INST-MFA was performed under the assumption that the metabolism is steady-state (Supplementary Method 4 with steady-state assumption validated below). The selection of labeling data for INST-MFA modeling and tests for several network models are described in Supplementary Method 4. A subset of key measured labeling data and the labeling kinetics simulated by the best-fit INST-MFA flux values are shown in Supplementary Figure 1 and the detailed fits of the best-fit models are shown in Supplementary Data 3.

Manipulating O_2 condition had a large and significant effect on v_o (2.60-26.37 μmol g^{-1} FW hr^{-1}) and a smaller but significant effect on v_c (53.36-79.70 μmol g^{-1} FW hr^{-1}, Fig. 1, 95% confidence intervals of the best-fit fluxes are shown in Supplementary Figure 2 and 3 and Supplementary Data 4). The rate of starch and sucrose synthesis decreased significantly with increasing rates of photorespiration (Fig. 1 and Supplementary Data 4). Direct measurement of the allocation of photo-assimilated C using $^{14}CO_2$ labelling showed that rates of starch and sucrose synthesis are strongly correlated with A (Supplementary Figure 4 and Supplementary Method 2).

The INST-MFA revealed the export rates of photorespiratory serine and glycine from the photorespiratory pathway at ambient CO_2 partial pressures (Fig. 1). The serine export rate to alternative sinks increased from 3.61 to 7.02 μmol g^{-1} FW hr^{-1} at high rates of photorespiration, but it decreased to 0.02 μmol g^{-1} FW hr^{-1} at low photorespiration rates. The export of glycine to alternative sinks was less than 0.01 μmol g^{-1} FW hr^{-1} at three conditions, much lower than that of serine. A portion of the export of amino acids from photorespiration, the removal of glycine or serine through phloem, was estimated based on the output flux to phloem and the output flux ratios of amino acids and sucrose measured in vascular exudate (Supplementary Table 2 and Supplementary Method 4). The removal rates of glycine or serine through the phloem were small relative to the total export, between 0.03 to 0.38 μmol g^{-1} FW hr^{-1} at various photorespiratory conditions (Fig. 1). The total amount of C leaving the photorespiratory pathway as serine scaled with the rate of photorespiration. At high photorespiration (40% O_2), 41% of the photorespiratory C influx (52.8 μmol C g^{-1} FW hr^{-1}) was exported as serine (at a rate of 21.5 μmol C g^{-1} FW hr^{-1}). The percentage of photorespiratory C leaving as serine was 32% at normal photorespiration (21% O_2) and 23% at low photorespiration (2% O_2). These data indicate that 23-41% of the photorespiratory C could be exported from the pathway as serine under physiologically relevant CO_2 partial pressures. The INST-MFA model was also run with glycerate labelling data and allowing glycerate export from the photorespiratory pathway. This extended model predicted that glycerate and glycine export rate was slow (< 0.1 μmol g^{-1} FW hr^{-1} in all oxygen conditions), while the serine export rate was slow at low photorespiration and rose at normal and high photorespiration (<0.1, 3.7 and 7.0 μmol g^{-1} FW hr^{-1} in 2%, 21%, and 40% O_2 respectively) (see Supplemental Method 4).

Estimating photorespiratory C export using CO_2 response of A

The export of photorespiratory C to amino acid synthesis or alternative metabolism accounts for the behavior of A at high CO_2 partial pressures in leaf photosynthesis models [13,15]. Using this approach, we estimated the fraction of C that leaves the photorespiratory pathway as glycine (α_G) and serine (α_S) using the measured CO_2 response of A at ambient O_2 and high light (~1000 μmol m^{-2} s^{-1}) fitted with the photosynthetic model over the triose phosphate utilization (TPU)-limited range to compare to the INST-

MFA results (Fig. 2). The high-CO_2 portion of the curve in orange, where TPU limits CO_2 assimilation, showed the characteristic curve that is only explained by amino acid removal from photorespiration [13,35]. This curvature was used to fit a resultant α_G and α_S of 0.01 and 0.45, indicating that the C flow out of photorespiration was primarily in the form of serine, consistent with the estimates ($\alpha_G < 0.01$ and $\alpha_S = 0.32$) calculated from the INST-MFA (Fig. 1).

Metabolic responses to low and high photorespiration

The absolute pool sizes of 38 central metabolic intermediates were measured in tobacco leaves exposed to varied photorespiratory conditions. Compared to the ambient O_2 condition, the metabolic changes at high photorespiration (40% O_2) and low photorespiration (2% O_2) were modest (Fig. 3). Most metabolites had insignificant changes in pool size during the short-term photorespiratory changes (Fig. 3 shows the mean fold-changes of the pool size between 2% and 21% O_2 or between 40% and 21% O_2; Supplementary Data 5 shows the absolute concentrations under the three oxygen conditions). The most significantly altered metabolites were photorespiratory intermediates (glycine, glycolate and glyoxylate), alanine, and ADPG (Supplementary Data 5). Many photorespiratory intermediates (glycine, serine, glycerate, glycolate and glyoxylate) were far from fully labelled even at high photorespiratory condition (Supplementary Figure 5). The average ^{13}C enrichment of these metabolites reached between 10% and 75% following 30 min of $^{13}CO_2$ labeling (Supplementary Figure 5), indicating that these intermediates exist in multiple subcellular pools with an active pool being involved in photorespiration and other pools (presumably in the vacuole [25]) not involved in photorespiration. The active and inactive pools of glycine were estimated using the measured total pool size and the dilution parameters from the INST-MFA (Supplementary Data 4 and 5). The extent of changes in glycine was much greater in the active pool (15-fold) than in the total pool (4-fold) (Fig. 4). These data support the steady-state assumption of INST-MFA (Supplementary Figure 6).

These data highlight the value of combining metabolite abundance with labeling and demonstrate the principle that in many cases changes in metabolite pool size do not directly translate into flux changes. For example, the pool size of 2PG was not significantly different between different oxygen conditions (Fig. 3 and Supplementary Data 5), but the ^{13}C labeling kinetics of 2PG were faster in high oxygen than in low oxygen (Supplementary Figure 1 and Supplementary Data 2), suggesting higher flux through rubisco oxygenation. This highlights that time-dependent labeling profiles are more informative indicators for flux rather than changes in pool sizes and that inferring flux from pool sizes alone can lead to inaccurate interpretations.

Photorespiration under non-steady state

Quantifying the steady-state active pool size of glycine at low and high photorespiratory conditions helped determine how much the size of glycine pools constrain net gas exchange during photorespiratory transients. To do this, *A* during O_2 transients was measured when tobacco leaves were exposed to 2% O_2 until the steady-state and then switched to 40% O_2. During the low-to-high O_2 transient, *A* did not instantly reach a new steady state at 40% O_2 but gradually declined at an exponential rate for ~2 min until the new steady-state was reached (Fig. 5). The extra C gained or lost during the transient in the decrease (or increase) in *A* as compared to how much C would be fixed with an instant transition to the new steady state was defined as the "C lag", which can be quantified by integrating the area between the fitted curve of *A* and a baseline of *A* at the new steady state (Fig. 5a). During the transition from 2% O_2 to 40% O_2, the total glycine pool increased by 30.8 ± 2.4 μmol m^{-2} based on the differences in steady-state levels (after 30 min acclimation to high or low oxygen) between high and low oxygen levels (Fig 4) or 20.8 ± 6.2 μmol m^{-2} based on the initial build-up of glycine pool after switching oxygen for 60 s when the gas exchange transient is near complete (Supplementary Figure 7), accounting for 20-30% of the total C lag (50.4 ± 1.7 μmol m^{-2}) as the accumulated glycine would otherwise be metabolized by the downstream glycine decarboxylase reaction (2 mol of glycine yielding 1 mol of CO_2). The build-up of the active glycine pool based on the steady-state measurement (25.7 ± 3.4 μmol m^{-2}, Fig 4) accounted for ~25% of the total C lag. When looking at the transition from 40% O_2 to 2% O_2, the lag in the photosynthetic increase resulted in loss of C represented by the shaded area (Fig. 5b). The reduction of the active glycine pool based on the steady-state measurement explained ~15% of this total C lag (83.9 ± 3.8 μmol m^{-2}). Note that the change in concentrations in response to O_2 treatment is negligible and small in other metabolites upstream of glycine (i.e. 2PG, glycolate and glyoxylate, Fig. 5), further indicating glycine is the primary metabolic pool impacting this transient response.

Discussion

Impact of photorespiratory flux changes on C and N metabolism

Our INST-MFA indicates that C was exported from photorespiration under ambient CO_2 partial pressures as serine at high rates. The INST-MFA-estimated fraction of serine export is 0.27-0.39 (95% confidence interval using the parameter continuation method) under ambient O_2 and CO_2 partial pressures (Supplementary Figure 2 and Supplementary Data 4), which is close to the 95% confidence interval of the value estimated using photosynthetic models fitted at high CO_2 partial pressures (0.38-0.51) (Fig. 2). Given these large export rates, where do these amino acids go? Prior studies have shown that glycine is incorporated into leaf protein when photorespiration is induced by low CO_2 [28,36], and almost all

photorespiratory glycine is routed to protein synthesis in water-stressed soybean leaves under high light and low CO_2 partial pressure [29]. Protein synthesis is not likely to explain all the amino acid export from photorespiration, since glycine and serine are present in similar proportions in total plant protein, but serine is exported at a much higher rate [37]. Past work also suggests that at least some photorespiratory serine and glycine is exported out of source leaves under photorespiratory conditions as is evident by an increased labeling in serine and glycine within the petiole when source leaves were labeled with $^{14}CO_2$ under elevated O_2 [38], but our vascular exudates indicated that removal from the leaf only accounted for a small percentage of the total amino acids exported from photorespiration. Photorespiratory glycine and serine are also required for the synthesis of various essential metabolites. For example. serine provides the carbon backbone for the synthesis of cysteine and tryptophan, which are further used to produce sulphur-containing compounds (*e.g.* S-adenosylmethionine) and indolic compounds (*e.g.* auxin and glucosinolates) [39,40]. Serine also is an important substrate for the biosynthesis of phosphatidylserine and sphingolipid that are critical to plant development and survival [41]. Glycine enhances the synthesis of glutathione (γ-Glu–Cys–Gly) as suggested by previous leaf feeding experiments [42]. Taken together, these findings indicate that photorespiration is an important source of amino acids for protein and metabolite synthesis and future work should work to resolve where specifically this serine goes within metabolism.

The increased fraction of photorespiratory C exported as amino acids with increased photorespiration in this study also helps explain the mechanistic link between photorespiration and N metabolism [5,43]. Large serine export fluxes diverted from photorespiration would need to be supplemented by equivalent *de novo* N assimilation. The *de novo* N assimilation rate would need to increase to support a higher total amount of photorespiratory C leaving as amino acids under higher photorespiratory condition. Supporting this hypothesis, plants under ambient photorespiration had ~10-30% higher N assimilation rates than those under low photorespiration (high CO_2 or low O_2) [8]. The coupling of N assimilation with photorespiration-derived glycine and serine has also been suggested from a dual labeling study with $^{13}CO_2$ and ^{15}N-ammonium nitrate [44]. In this 6-h labeling study, up to 50% of ^{15}N glycine and ^{15}N serine molecules were also ^{13}C enriched, probably due to large turnover glycine and serine associated with high flux rates of photorespiration, whereas many other amino acids were only ^{15}N-labelled because their ^{15}N-amino groups were not fixed onto ^{13}C-enriched C skeletons. Exporting glycine and serine from the photorespiratory pathway could enable plants to efficiently assimilate N onto C skeletons produced during photorespiration, also stimulating CO_2 uptake at high CO_2 [15].

The finding that large amounts of C leave photorespiration for other metabolisms and do not re-enter the C_3 cycle suggests some interesting hypotheses concerning the central purpose of photorespiration. Photorespiration is thought to be essential for returning C back into the C_3 cycle, but our flux values

indicate that only 43% returns following serine export, instead of the theoretically maximal 75% under 21% O_2. This rate of carbon removal is (large) relative to other fluxes in central metabolism, comprising 50% and 62% the C flux of starch and sucrose syntheses at 21% O_2. This indicates that the C_3 cycle is resilient against carbon removal and can replenish its own intermediates even under high rates of removal following rubisco oxygenation. This is not surprising given the ability for the C_3 cycle to operate even under high rates of rubisco oxygenation, like what occurs under 40% O_2 or elevated temperatures. Conceptually this is similar to carbon removal from the C3 cycle to other metabolisms like sucrose and starch. These findings favor the hypothesis that the major roles of photorespiration are to provide C and N for downstream metabolism in addition to processing inhibitory byproducts of rubisco oxygenation. This would help explain why it interacts with so many other aspects of metabolism. It may also explain why photorespiration is maintained in all oxygenic phototrophs, and is even essential (albeit in reduced amounts) in plant species with an efficient carbon concentrating mechanism in addition to its role in processing 2PG [45].

Role of glycine in photorespiration and *A* during transients

Our metabolomics analyses identified a significant correlation between photorespiratory rate and glycine pool size, which is large enough to explain much of the transient response of *A* to changing photorespiratory conditions. The metabolically active glycine pools inferred from the dilution parameters in our INST-MFA changed 15-fold when comparing low and high photorespiration (Fig. 4). Our gas exchange data showed that during the low-to-high O_2 transient, the concomitant accumulation of active glycine pools that are not decarboxylated accounted for ~25% of the excess CO_2 fixed (Fig. 5a). Interestingly, the relaxation of active glycine pools accounts for a slightly smaller ~15% of the excess CO_2 lost during the high-low O_2 transient (Fig. 5b). These findings indicate a unique connection between the accumulation of a single metabolite and the subsequent effects to *A*. Further research is needed to determine what the remaining determinants of the acclimation of net assimilation between photorespiratory conditions are and how well these findings translate to other changes in photorespiratory rate, like under fluctuating light [46].

These findings support a hypothesis as to the role of glycine in photorespiration as a “safe” buffering metabolite in a dynamic pathway. The biochemical structure and kinetics of photorespiration may be configured to accumulate glycine so that other upstream or downstream intermediates do not change too rapidly or build up to inhibitory or cytotoxic concentrations. Photorespiratory intermediates downstream of glycine were not significantly changed at varying photorespiratory conditions (Fig. 3). Many other

studies have shown that glycine is the most drastically changed photorespiratory intermediates upon photorespiratory pressures [17,18,20,21,47], suggesting that glycine is a well-tolerated metabolite in plant cells. The build-up of glycine may also suggest that photorespiration has been optimized to delay the release of ammonium until there is sufficient glutamine synthetase/glutamate synthase activity to recapture the ammonium released from the GDC reaction. In contrast, other photorespiratory intermediates are riskier to accumulate. For example, the cytotoxicity of 2-PG, glycolate, glyoxylate, and serine suggests tight regulation of their intracellular concentrations [45,48–52]. The toxicity of glycolate and glyoxylate may be more nuanced however, since transformants expressing novel photorespiratory genes had ~3 and ~8 fold higher concentrations of glycolate and glyoxylate with no obvious cytotoxic effects [53]. In addition to these cytotoxic intermediates, serine may act as a signal for the transcriptional regulation of photorespiration-related genes, as external supply of serine induces transcriptional deregulation so pool sizes would need to be relatively buffered to prevent a hyper-sensitivity to short-term changes in photorespiratory flux [54]. Furthermore, accumulated glycerate could exert a feed-back effect on photosynthesis by blocking the stromal fructose-1,6-bisphosphatase [55]. Of all the photorespiratory intermediates, glycine therefore appears to be the most inert to metabolism and therefore a waypoint to help safely navigate dynamic changes in flux.

The transient build-up in glycine pools when switching from low to high photorespiratory condition indicates that the capacity of the downstream photorespiratory enzyme GDC may not be sufficient to process large changes in glycine influx under non-steady state conditions. Limiting GDC activity even by ~50% leads to a 100-fold accumulation of glycine during the day, while stimulating GDC activity leads to a ~40% reduction in steady-state level of glycine [56,57]. Moreover, upregulating GDC activity improves plant performance both in the laboratory and field conditions [57,58], suggesting its key role in controlling photorespiratory flux. While GDC is normally not limited by its substrate glycine and NAD^+, the efficient operation of GDC requires maintaining low levels of its product NADH, which may accumulate during rapid changes in flux through GDC [59]. The mitochondrial TRX system has been proposed to be important in the redox regulation of GDC under fluctuating light, adding to its potential role under transient conditions[60,61].

An additional explanation for the increase in glycine pools relative to serine during increasing photorespiration is the need to maintain appropriate concentration gradients to drive transport of these metabolites between the mitochondrion and peroxisome. While these transporters are not yet identified, they must facilitate large fluxes and are most likely driven by concentration gradients that are proportional to their fluxes [62]. Glycine flux into the mitochondria is twice as large as serine flux out since the GDC/serine hydroxymethyltransferase reactions require two glycine per serine produced and

assuming a "closed cycle" of photorespiration. Since higher transport gradients would translate to higher leaf-level pool sizes of metabolites, the differences in flux may also help explain the high build-up of glycine relative to serine.

Methods

Plant material. Tobacco (*Nicotiana tabacum*) plants were grown in a growth chamber under an 18-h day/6-h night photoperiod at a light intensity of 100 μmol m^{-2} s^{-1}, day/night temperatures of 23°C/18°C, and relative humidity of 60%. All experiments were performed on the fully expanded source leaves of 8-week-old plants.

Gas exchange and $^{13}CO_2$ labeling system. Leaf gas exchange measurements under controlled $O_2/CO_2/N_2$ conditions were performed using a LI-6800 (LI-COR Biosciences, USA) with a fast atmospheric switching and quenching system as described previously [33]. Leaves were equilibrated and monitored in the cuvette at 40 Pa $^{12}CO_2$ levels with three O_2/N_2 conditions (2% O_2 / 98% N_2, 21% O_2/ 79% N_2, and 40% O_2/ 60 % N_2), light intensity of 100 μmol photon m^{-2} s^{-1}, leaf temperature of 25 °C, and relative humidity of 70%. $^{13}CO_2$ labeling was performed after 20-30 min of acclimation to reach a photosynthetic steady-state. Illuminated leaves were incubated at 0, 0.5, 1, 2, 2.5, 3, 5, 7, 10, 15, and 30 min with $^{13}CO_2$-containing gas mixture ([40 Pa] $^{13}CO_2$ with each O_2/N_2 condition) before quenching. Pseudo-steady state metabolism was assumed during the labeling period at each oxygen condition (Supplementary Figure 6). Detailed descriptions of tissue harvesting and quenching for metabolic analyses are shown in Supplementary Method 1.

Metabolite labeling and concentration. The extraction and analytical procedures for quantifying metabolite labeling and concentration were similar to the method described previously [33]. Gas chromatography-mass spectrometry (GC-MS) was used to analyze amino acids, organic acids, and sugars. Ion-pair chromatography-tandem mass spectrometry (IPC-MS/MS) was used to analyze the phosphorylated intermediates in C_3 cycle. Anion exchange chromatography-tandem mass spectrometry (AEC-MS/MS) was used to analyze nucleotide sugars and additional phosphorylated intermediates. Detailed descriptions of the extraction and mass spectrometry analyses are shown in Supplementary Method 1 and Supplementary Data 6. Abbreviations of metabolites are shown in Supplementary Data 7.

Measurements of external fluxes. Rates of starch and sucrose synthesis were measured by the steady state pulse-chase labeling of $^{14}CO_2$ as described previously [35] with slight modifications (Supplementary Method 2). Rates of rubisco carboxylation and oxygenation were calculated as described earlier using gas

exchange measurements [2], with the required biochemical and diffusional parameters experimentally estimated by gas exchange and isotope analysis (see Supplementary Method 3 for details). The output flux ratios of amino acids and sucrose were estimated by measuring steady-state levels of sucrose and amino acids in vascular exudate as described earlier [26,33]. Detailed descriptions of exudate collection were described in Supplementary Method 1.

Metabolic network and flux determination. The network model used for flux determination was modified from published reaction models [26,33,34] (Supplementary Data 1). INST-MFA was performed using the elementary metabolite unit (EMU)-based software INCA (version 1.8) [63] ran within MATLAB 2018b (Mathworks, USA). Model formulation details are described in Supplementary Method 4 and the INCA model files are included in Supplementary Data 8. Metabolic fluxes were estimated by iteratively minimizing the sum of squared residuals (SSR) between the experimentally measured and simulated isotopic labeling patterns and measured external rates, using a Levenberg-Marquardt optimization algorithm [64]. Each flux estimation was repeated a minimum of 100 times from random initial values to find best-fit estimates. All results were subjected to a χ^2-statistical test for goodness-of-fit and the 95% confidence intervals were computed for all estimated fluxes using two independent methods. A parameter continuation method was used to evaluate the sensitivity of SSR to flux variations [65]. A Monte Carlo method was used to estimate flux distributions based on 3,000 sets of external flux measurements and MID data perturbed by normally distributed noise with the measured SD. The parameter continuation and Monte Carlo simulations were computed in parallel using a high-performance computing environment (Institute for Cyber-Enabled Research at Michigan State University) and a cloud computing environment (Microsoft Azure). The cloud-based workflow to run the Monte Carlo simulations can be found at https://github.com/codexf/MFA_Cloud_Computing.

Estimating photorespiratory C export using CO_2 response of *A*. A/C_c curves were measured with a LI-6800 at a light intensity of 1000 μmol photon m^{-2} s^{-1} and a leaf temperature of 25 °C. The sequence of reference CO_2 partial pressures was 40, 5, 7.5, 10, 15, 20, 25, 30, 35, 40, 45, 50, 60, 80, 100, and 120 Pa. Photosynthetic parameters, including the C exported from photorespiration as glycine (α_G) or serine (α_S), were estimated from the A/C_i curves using the modified Farquhar, von Caemmerer and Berry (FvCB) biochemical model of photosynthesis fitted against rubisco, RuBP-regeneration, triose-phosphate use limitations, α_G and (α_S) [15,66,67]. Data and custom scripts can be found at https://github.com/codexf/Modeling_Photosynthesis.

Transient response of *A* to changes in O_2 mole fraction. Dynamic photosynthesis was recorded using a LI-6800 with 2-s intervals. The leaves were illuminated (100 μmol m^{-2} s^{-1}) in 40 Pa CO_2 levels (CO_2 injector manually controlled) with either high O_2 (40% O_2 / 60% N_2) or low O_2 (2% O_2 / 98% N_2). When

the steady-state rate of *A* had been achieved, the cuvette was switched to low or high O_2 and leaves were left to reach a new steady-state rate of *A*. The time course data were fitted using one-phase exponential functions and the integrated area between the fitted curve and the baseline of the new steady-state *A* was calculated to estimate the total C lag during the transients. Data and custom scripts can be found at https://github.com/codexf/Modeling_Photosynthesis.

Data availability

All data used in this study are provided as Supporting Information of the article or available upon request. Gas exchange data for modeling the photosynthetic responses to carbon dioxide concentration and photosynthetic responses during oxygen transients can be found on GitHub at https://github.com/codexf/Modeling_Photosynthesis.

Code availability

Custom scripts for modeling the photosynthetic responses to carbon dioxide concentration and photosynthetic responses during oxygen transients can be found on GitHub at https://github.com/codexf/Modeling_Photosynthesis. A cloud-based workflow to run the Monte Carlo simulations for computing confidence intervals of metabolic fluxes can be found on GitHub at https://github.com/codexf/MFA_Cloud_Computing.

Acknowledgements

We thank Aikaari Ryce at Michigan State University (MSU) for experimental assistance; Thomas D. Sharkey (MSU) for providing lab space and guidance for performing the $^{14}CO_2$ labeling experiments; Yuan Xu and Yair Shachar-Hill (MSU) for helpful discussions on INST-MFA; James Klug and Cody Keilen (MSU Growth Chamber Facility) for plant maintenance; A. Daniel Jones, Lijun Chen, and Casey Johnny (MSU Mass Spectrometry and Metabolomics Core Facility) for advising metabolomics analyses; Patrick Bills (MSU IT Services), Xiaoge Wang, and Mahmoud Parvizi (MSU Institute for Cyber-Enabled Research) for consulting on cloud computing and high-performance computing. The computational work was supported in part through the high-performance computing cluster and services provided by the Institute for Cyber-Enabled Research at MSU. The computational work was also supported in part through MSU's Institute for Cyber-Enabled Research Cloud Computing Fellowship, with computational

resources and services provided by Information Technology Services and the Office of Research and Innovation at MSU. We also thank Jamey Young for making INCA accessible and Hilary Stewart Williams for help establishing the online isotope analysis system. This work was supported by the U.S. Department of Energy Office of Science, Basic Energy Sciences under Award DE- FG02-91ER20021 (BJW, XF, and SEW). This material is also based upon work supported in part by the Great Lakes Bioenergy Research Center, U.S. Department of Energy, Office of Science, Office of Biological and Environmental Research under Award Number DE-SC0018409 (BJW) and the National Science Foundation under Grant No. 2030337 (BJW and LMG). We also thank the constructive feedback from three anonymous reviewers, which greatly increased the quality and strength of this work.

Author contributions

BJW and XF designed the experiments. XF carried out the bulk of the experiments and analyzed the results. SEW advised and assisted the $^{14}CO_2$ experiments to measure starch and sucrose partitioning. LG performed the isotope analysis to measure gas exchange parameters. XF wrote the manuscript with contributions from all the authors. BJW serves as the author responsible for contact and ensures communication.

Competing interests

The authors declare no competing interests.

Figure legends

Fig. 1: Central carbon assimilatory metabolic fluxes in tobacco leaves exposed to varying O_2 conditions. Fluxes were estimated by ^{13}C INST-MFA using the metabolic network model and experimental inputs including mass isotopologue distributions of measured metabolites, the net CO_2 assimilation rate, rates of rubisco carboxylation and oxygenation, rates of starch and sucrose synthesis, and output flux ratios of amino acids and sucrose. Best-fit flux estimates are shown in numbers and corresponding variable width of arrows. Arrows in blue indicate reactions constrained (not fixed) based on the experimental measurements (Supplementary Table 1). Flux units are expressed as μmol molecule g^{-1} FW hr^{-1} (for the conversion to μmol carbon g^{-1} FW hr^{-1}, multiply the presented values by the number of carbons in the molecule). Metabolites compartmentalized to the plastid and cytosol are denoted by (".p") and (".c") respectively. Abbreviations are shown in Supplementary Data 7.

Fig. 2: The response of A to the chloroplastic CO_2 concentration (Cc) in tobacco leaves exposed to 21% O_2 under high light (1000 μmol m^{-2} s^{-1}). Measured A are presented as dots with error bars (mean ± SD, n = 9 biologically independent leaves) fitted with the modified Farquhar, von Caemmerer and Berry (FvCB) biochemical model of photosynthesis with two terms α_G and α_S, where α_G is the proportion of the carbon exported from the photorespiratory pathway as glycine, and α_S the proportion of the carbon exported from photorespiration as serine (see Method section: *Estimating photorespiratory C export using CO_2 response of A*). The parameter values obtained from the individual fits are shown as mean ± SD (n = 9 biologically independent leaves), including the maximum rubisco carboxylation rate (V_{cmax}), the maximum rate of electron transport (J), the rate of triose phosphate export from the chloroplast (T_p), α_G and α_S. The curves represent Rubisco (red), RuBP (green), and TPU (orange) limitation.

Fig. 3: Metabolic pool size alterations in response to photorespiratory conditions. Tobacco leaves were exposed to the three O_2/N_2 conditions (all at 40 Pa $^{12}CO_2$ levels) in the LI-6800 cuvette for 30 min until quenching with liquid nitrogen under illumination. Leaves acclimated to 2% O_2 and 40% O_2 were compared to the ambient O_2 condition respectively and the steady-state pool sizes of the identified metabolites (plotted on the y-axis) were determined using GC-MS and LC-MS/MS. The x-axis plots the log2-transformed relative ratio of abundance of each metabolite in the leaves exposed to 2% O_2 (blue) or 40% O_2 (red) normalized to the same metabolite in the leaves exposed to 21% O_2. Results are presented as dots with error bars (mean ± SEM, n = 7 or 8 biologically independent leaves). Asterisk represents a significant difference between two conditions (Benjamini-Hochberg procedure was used to control the false discovery rate at 0.05 for multiple *t*-tests including all metabolites). Supplementary Data 5 presents the absolute concentration of each metabolite under different oxygen conditions with the results of one-way ANOVA followed by Tukey's test for multiple pairwise comparisons among the three oxygen conditions per metabolite. Abbreviations of metabolites are shown in Supplementary Data 7.

Fig. 4: Active and inactive pools of glycine at varying O_2 levels. Tobacco leaves were exposed to the three O_2/N_2 conditions (all at 40 Pa $^{12}CO_2$ levels) in the LI-6800 cuvette for 30 min until quenching with liquid nitrogen under illumination. Steady-state pool sizes of glycine were determined using GC-MS. The proportion of active (gray) and inactive (white) pools of glycine were estimated using the dilution parameters in INST-MFA modeling. Data are presented as box plots (center line at the median, upper bound at 75th percentile, lower bound at 25th percentile) with whiskers extended to the extreme data point ≤ 1.5 × interquartile range from the edge of the box (n = 7 or 8 biologically independent leaves). Different letters above the data boxes denote statistically significant differences among the three conditions for active glycine pools (uppercase letters) and inactive glycine pools (lowercase letters) at $P <$ 0.05 (one-way ANOVA followed by Tukey's test for multiple pairwise comparisons). For active glycine

pools, the P values for Tukey multiple comparisons of means are 0.0006 (2% O2 - 21% O2), <0.0001 (2% O2 - 40% O2), and 0.0042 (21% O2 - 40% O2). For inactive glycine pools, the P values for Tukey multiple comparisons of means are 0.0260 (2% O2 - 21% O2), 0.0138 (2% O2 - 40% O2), and 0.9511 (21% O2 - 40% O2).

Fig. 5: Dynamics of net CO_2 assimilation rate (A) during oxygen transients from 2% O_2 to 40% O_2 (a) and from 40% O_2 to 2% O_2 (b). The leaves were acclimated in a LI-6800 cuvette at low O_2 or high O_2 for 30 min to reach the photosynthetic steady-state. Upon switching to the opposite oxygen condition, A changed drastically due to slow gas mixing and returned to the previous steady state within ~10 s. The time when the previous steady state was reached after switching oxygen was set to zero for the convenience of curve fitting. Data points of different colors correspond to independent time-course measurements on ten different plants. Lines of different colors represent the fitted curves of a one-phase exponential function for individual replicates. Integrated area between the fitted curve and the baseline of new steady state for a represented replicate is presented in the inserts. The integrated area obtained from the ten individual fits are shown as mean ± SD (n = 10 biologically independent leaves).

References

1. Walker, B. J., Kramer, D. M., Fisher, N. & Fu, X. Flexibility in the energy balancing network of photosynthesis enables safe operation under changing environmental conditions. *Plants* **9**, (2020).
2. Bauwe, H., Hagemann, M. & Fernie, A. R. Photorespiration: players, partners and origin. *Trends Plant Sci.* **15**, 330–336 (2010).
3. Bauwe, H., Hagemann, M., Kern, R. & Timm, S. Photorespiration has a dual origin and manifold links to central metabolism. *Curr. Opin. Plant Biol.* **15**, 269–275 (2012).
4. Hanson, A. D. & Roje, S. One-carbon metabolism in higher plants. *Annu. Rev. Plant Biol.* **52**, 119–137 (2001).
5. Bloom, A. J. Photorespiration and nitrate assimilation: A major intersection between plant carbon and nitrogen. *Photosynth. Res.* **123**, 117–128 (2015).
6. Tcherkez, G. *et al.* Respiratory metabolism of illuminated leaves depends on CO2 and O2 conditions. *Proc. Natl. Acad. Sci. U. S. A.* **105**, 797–802 (2008).
7. Rachmilevitch, S., Cousins, A. B. & Bloom, A. J. Nitrate assimilation in plant shoots depends on photorespiration. *Proc. Natl. Acad. Sci. U. S. A.* **101**, 11506–11510 (2004).
8. Bloom, A. J., Burger, M., Asensio, J. S. R. & Cousins, A. B. Carbon dioxide enrichment inhibits nitrate assimilation in wheat and arabidopsis. *Science (80-.).* **328**, 899–903 (2010).
9. Cotrufo, M. F., Ineson, P. & Scott, A. Elevated CO2 reduces the nitrogen concentration of plant tissues. *Glob. Chang. Biol.* **4**, 43–54 (1998).
10. Abadie, C., Blanchet, S., Carroll, A. & Tcherkez, G. Metabolomics analysis of postphotosynthetic effects of gaseous O2 on primary metabolism in illuminated leaves. *Funct. Plant Biol.* **44**, 929–940 (2017).
11. Tcherkez, G. *et al.* Short-term effects of CO2 and O2 on citrate metabolism in illuminated leaves. *Plant, Cell Environ.* **35**, 2208–2220 (2012).
12. Hodges, M. *et al.* Perspectives for a better understanding of the metabolic integration of photorespiration within a complex plant primary metabolism network. *Journal of Experimental*

Botany vol. 67 3015–3026 (2016).
13. Harley, P. C. & Sharkey, T. D. An improved model of C3 photosynthesis at high CO2: Reversed O2 sensitivity explained by lack of glycerate reentry into the chloroplast. *Photosynth. Res.* **27**, 169–178 (1991).
14. Busch, F. A. & Sage, R. F. The sensitivity of photosynthesis to O2 and CO2 concentration identifies strong Rubisco control above the thermal optimum. *New Phytol.* **213**, 1036–1051 (2017).
15. Busch, F. A., Sage, R. F. & Farquhar, G. D. Plants increase CO2 uptake by assimilating nitrogen via the photorespiratory pathway. *Nat. Plants* **4**, 46–54 (2018).
16. McClain, A. M. & Sharkey, T. D. Triose phosphate utilization and beyond: From photosynthesis to end product synthesis. *J. Exp. Bot.* **70**, 1755–1766 (2019).
17. Eisenhut, M. *et al.* Photorespiration is crucial for dynamic response of photosynthetic metabolism and stomatal movement to altered CO2 availability. *Mol. Plant* **10**, 47–61 (2017).
18. Timm, S. *et al.* High-to-low CO2 acclimation reveals plasticity of the photorespiratory pathway and indicates regulatory links to cellular metabolism of Arabidopsis. *PLoS One* **7**, e42809 (2012).
19. Wingler, A. *et al.* The role of photorespiration during drought stress: An analysis utilizing barley mutants with reduced activities of photorespiratory enzymes. *Plant, Cell Environ.* **22**, 361–373 (1999).
20. Abadie, C., Bathellier, C. & Tcherkez, G. Carbon allocation to major metabolites in illuminated leaves is not just proportional to photosynthesis when gaseous conditions (CO2 and O2) vary. *New Phytol.* **218**, 94–106 (2018).
21. Abadie, C., Boex-Fontvieille, E. R. A., Carroll, A. J. & Tcherkez, G. In vivo stoichiometry of photorespiratory metabolism. *Nat. plants* **2**, 15220 (2016).
22. Abadie, C. & Tcherkez, G. 13C isotope labelling to follow the flux of photorespiratory intermediates. *Plants* **10**, 1–12 (2021).
23. Bao, H. *et al.* Catalase protects against nonenzymatic decarboxylations during photorespiration in Arabidopsis thaliana. *Plant Direct* **5**, (2021).
24. Tcherkez, G. *et al.* Leaf day respiration: low CO2 flux but high significance for metabolism and carbon balance. *New Phytol.* **216**, 986–1001 (2017).
25. Szecowka, M. *et al.* Metabolic fluxes in an illuminated Arabidopsis rosette. *Plant Cell* **25**, 694–714 (2013).
26. Ma, F., Jazmin, L. J., Young, J. D. & Allen, D. K. Isotopically nonstationary 13C flux analysis of changes in Arabidopsis thaliana leaf metabolism due to high light acclimation. *Proc. Natl. Acad. Sci. U. S. A.* **111**, 16967–16972 (2014).
27. Abadie, C., Lalande, J., Limami, A. M. & Tcherkez, G. Non-targeted 13C metabolite analysis demonstrates broad re-orchestration of leaf metabolism when gas exchange conditions vary. *Plant Cell Environ.* **44**, 445–457 (2021).
28. Cegelski, L. & Schaefer, J. NMR determination of photorespiration in intact leaves using in vivo 13CO2 labeling. *J. Magn. Reson.* **178**, 1–10 (2006).
29. Dirks, R. C., Singh, M., Potter, G. S., Sobotka, L. G. & Schaefer, J. Carbon partitioning in soybean (Glycine max) leaves by combined 11C and 13C labeling. *New Phytol.* **196**, 1109–1121 (2012).
30. Ratcliffe, R. G. & Shachar-Hill, Y. Measuring multiple fluxes through plant metabolic networks. *Plant J.* **45**, 490–511 (2006).
31. Chu, K. L. *et al.* Metabolic flux analysis of the non-transitory starch tradeoff for lipid production in mature tobacco leaves. *Metab. Eng.* **69**, 231–248 (2022).
32. Treves, H. *et al.* Carbon flux through photosynthesis and central carbon metabolism show distinct patterns between algae, C3 and C4 plants. *Nat. Plants* **8**, 78–91 (2022).
33. Xu, Y., Fu, X., Sharkey, T. D., Shachar-Hill, Y. & Walker, B. J. The metabolic origins of non-photorespiratory CO2 release during photosynthesis: A metabolic flux analysis. *Plant Physiol.*

186, 297–314 (2021).
34. Xu, Y., Wieloch, T., Kaste, J. A. M., Shachar-Hill, Y. & Sharkey, T. D. Reimport of carbon from cytosolic and vacuolar sugar pools into the Calvin-Benson cycle explains photosynthesis labeling anomalies. *Proc. Natl. Acad. Sci. U. S. A.* **119**, (2022).
35. Sharkey, T. D., Berry, J. A. & Raschke, K. Starch and sucrose synthesis in Phaseolus vulgaris as affected by light, CO2, and abscisic acid. *Plant Physiol.* **77**, 617–620 (1985).
36. Cegelski, L. & Schaefer, J. Glycine metabolism in intact leaves by in vivo13C and 15N labeling. *J. Biol. Chem.* **280**, 39238–39245 (2005).
37. Heinemann, B., Künzler, P., Eubel, H., Braun, H. P. & Hildebrandt, T. M. Estimating the number of protein molecules in a plant cell: protein and amino acid homeostasis during drought. *Plant Physiol.* **185**, 385–404 (2021).
38. Madore, M. & Grodzinski, B. Effect of oxygen concentration on 14C-photoassimilate transport from leaves of Salvia splendens L. *Plant Physiol.* **76**, 782–786 (1984).
39. Takahashi, H., Kopriva, S., Giordano, M., Saito, K. & Hell, R. Sulfur assimilation in photosynthetic organisms: Molecular functions and regulations of transporters and assimilatory enzymes. *Annu. Rev. Plant Biol.* **62**, 157–184 (2011).
40. Radwanski, E. R. & Last, R. L. Tryptophan biosynthesis and metabolism: Biochemical and molecular genetics. *Plant Cell* **7**, 921–934 (1995).
41. Ros, R., Muñoz-Bertomeu, J. & Krueger, S. Serine in plants: Biosynthesis, metabolism, and functions. *Trends Plant Sci.* **19**, 564–569 (2014).
42. Noctor, G., Arisi, A. C. M., Jouanin, L. & Foyer, C. H. Photorespiratory glycine enhances glutathione accumulation in both the chloroplastic and cytosolic compartments. *J. Exp. Bot.* **50**, 1157–1167 (1999).
43. Foyer, C. H., Bloom, A. J., Queval, G. & Noctor, G. Photorespiratory metabolism: Genes, mutants, energetics, and redox signaling. *Annu. Rev. Plant Biol.* **60**, 455–484 (2009).
44. Gauthier, P. P. G. *et al.* In folio isotopic tracing demonstrates that nitrogen assimilation into glutamate is mostly independent from current CO2 assimilation in illuminated leaves of Brassica napus. *New Phytol.* **185**, 988–999 (2010).
45. Zelitch, I., Schultes, N. P., Peterson, R. B., Brown, P. & Brutnell, T. P. High glycolate oxidase activity is required for survival of maize in normal air. *Plant Physiol.* **149**, 195–204 (2009).
46. Fu, X. & Walker, B. J. Dynamic response of photorespiration in fluctuating light environments. *J. Exp. Bot.* (2022) doi:https://doi.org/10.1093/jxb/erac335.
47. Hitz, W. D. & Stewart, C. R. Oxygen and carbon dioxide effects on the pool size of some photosynthetic and photorespiratory intermediates in soybean (Glycine max [L.] Merr.). *Plant Physiol.* **65**, 442–446 (1980).
48. Flügel, F. *et al.* The photorespiratory metabolite 2-phosphoglycolate regulates photosynthesis and starch accumulation in Arabidopsis. *Plant Cell* **29**, 2537–2551 (2017).
49. Anderson, L. E. Chloroplast and cytoplasmic enzymes II. Pea leaf triose phosphate isomerases. *BBA - Enzymol.* **235**, 237–244 (1971).
50. Campbell, W. J. & Ogren, W. L. Glyoxylate inhibition of ribulosebisphosphate carboxylase/oxygenase activation in intact, lysed, and reconstituted chloroplasts. *Photosynth. Res.* **23**, 257–268 (1990).
51. Gonzalez-Moro, B., Lacuesta, M., Becerril, J. M., Gonzalez-Murua, C. & Munoz-Rueda, A. Glycolate accumulation causes a decrease of photosynthesis by inhibiting RUBISCO activity in maize. *J. Plant Physiol.* **150**, 388–394 (1997).
52. Kelly, G. J. & Latzko, E. Inhibition of spinach-leaf phosphofructokinase by 2-phosphoglycollate. *FEBS Lett.* **68**, 55–58 (1976).
53. South, P. F., Cavanagh, A. P., Liu, H. W. & Ort, D. R. Synthetic glycolate metabolism pathways

stimulate crop growth and productivity in the field. *Science (80-.).* **363**, (2019).
54. Timm, S. *et al.* Serine acts as a metabolic signal for the transcriptional control of photorespiration-related genes in Arabidopsis. *Plant Physiol.* **162**, 379–389 (2013).
55. Schimkat, D., Heineke, D. & Heldt, H. W. Regulation of sedoheptulose-1,7-bisphosphatase by sedoheptulose-7-phosphate and glycerate, and of fructose-1,6-bisphosphatase by glycerate in spinach chloroplasts. *Planta* **181**, 97–103 (1990).
56. Heineke, D., Bykova, N., Gardeström, P. & Bauwe, H. Metabolic response of potato plants to an antisense reduction of the P-protein of glycine decarboxylase. *Planta* **212**, 880–887 (2001).
57. Timm, S. *et al.* Glycine decarboxylase controls photosynthesis and plant growth. *FEBS Lett.* **586**, 3692–3697 (2012).
58. López-Calcagno, P. E. *et al.* Overexpressing the H-protein of the glycine cleavage system increases biomass yield in glasshouse and field-grown transgenic tobacco plants. *Plant Biotechnol. J.* **17**, 141–151 (2019).
59. Bykova, N. V., Møller, I. M., Gardeström, P. & Igamberdiev, A. U. The function of glycine decarboxylase complex is optimized to maintain high photorespiratory flux via buffering of its reaction products. *Mitochondrion* **19**, 357–364 (2014).
60. da Fonseca-Pereira, P. *et al.* Thioredoxin h2 contributes to the redox regulation of mitochondrial photorespiratory metabolism. *Plant Cell Environ.* **43**, 188–208 (2020).
61. Reinholdt, O. *et al.* Redox-regulation of photorespiration through mitochondrial thioredoxin O1. *Plant Physiol.* **181**, 442–457 (2019).
62. Eisenhut, M., Pick, T. R., Bordych, C. & Weber, A. P. M. Towards closing the remaining gaps in photorespiration - the essential but unexplored role of transport proteins. *Plant Biol.* **15**, 676–685 (2013).
63. Young, J. D. INCA: A computational platform for isotopically non-stationary metabolic flux analysis. *Bioinformatics* **30**, 1333–1335 (2014).
64. Young, J. D., Walther, J. L., Antoniewicz, M. R., Yoo, H. & Stephanopoulos, G. An elementary metabolite unit (EMU) based method of isotopically nonstationary flux analysis. *Biotechnol. Bioeng.* **99**, 686–699 (2008).
65. Antoniewicz, M. R., Kelleher, J. K. & Stephanopoulos, G. Determination of confidence intervals of metabolic fluxes estimated from stable isotope measurements. *Metab. Eng.* **8**, 324–337 (2006).
66. Farquhar, G. D., von Caemmerer, S. & Berry, J. A. A biochemical model of photosynthetic CO2 assimilation in leaves of C3 species. *Planta* **149**, 78–90 (1980).
67. Sharkey, T. D., Bernacchi, C. J., Farquhar, G. D. & Singsaas, E. L. Fitting photosynthetic carbon dioxide response curves for C3 leaves. *Plant, Cell Environ.* **30**, 1035–1040 (2007).

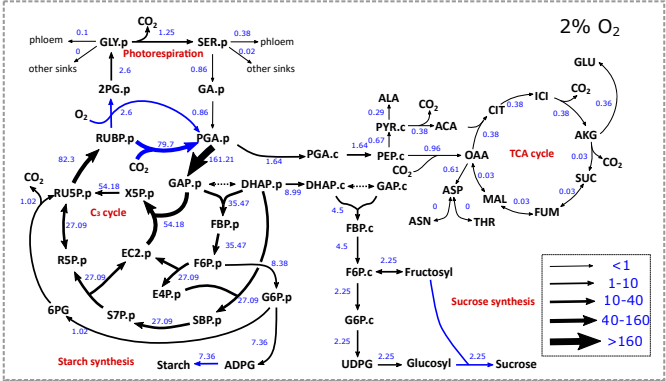
2% O2
Photorespiration
TCA cycle
C3 cycle
Sucrose synthesis
Starch synthesis
phloem
other sinks
GLY.p
SER.p
2PG.p
GA.p
RUBP.p
PGA.p
PGA.c
GAP.p
DHAP.p
DHAP.c
GAP.c
RU5P.p
X5P.p
R5P.p
EC2.p
F6P.p
E4P.p
S7P.p
SBP.p
G6P.p
6PG
Starch
ADPG
FBP.c
F6P.c
G6P.c
UDPG
Fructosyl
Glucosyl
Sucrose
PYR.c
ACA
ALA
CIT
ICI
AKG
SUC
FUM
MAL
OAA
PEP.c
ASP
ASN
THR
GLU
<1
1-10
10-40
40-160
>160

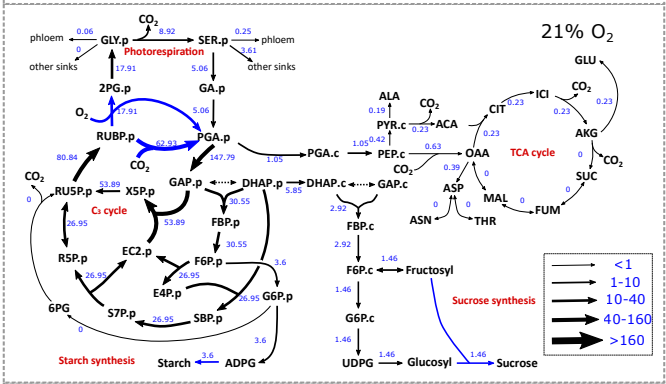
21% O2
Photorespiration
TCA cycle
C3 cycle
Sucrose synthesis
Starch synthesis
phloem
other sinks
GLY.p
SER.p
2PG.p
GA.p
RUBP.p
PGA.p
PGA.c
GAP.p
DHAP.p
DHAP.c
GAP.c
RU5P.p
X5P.p
R5P.p
EC2.p
F6P.p
E4P.p
S7P.p
SBP.p
G6P.p
6PG
Starch
ADPG
FBP.c
F6P.c
G6P.c
UDPG
Fructosyl
Glucosyl
Sucrose
PYR.c
ACA
ALA
CIT
ICI
AKG
SUC
FUM
MAL
OAA
PEP.c
ASP
ASN
THR
GLU
<1
1-10
10-40
40-160
>160

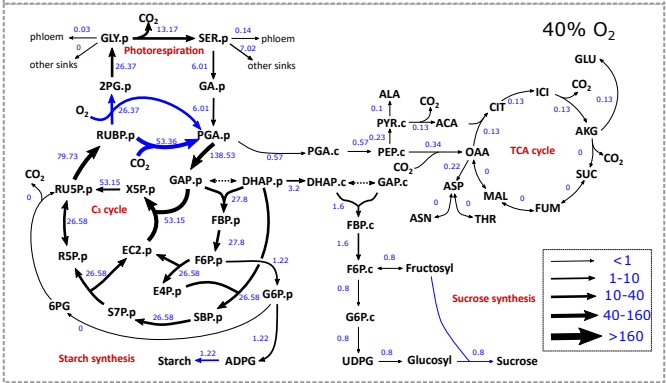
40% O2
Photorespiration
TCA cycle
C3 cycle
Sucrose synthesis
Starch synthesis
phloem
other sinks
GLY.p
SER.p
2PG.p
GA.p
RUBP.p
PGA.p
PGA.c
GAP.p
DHAP.p
DHAP.c
GAP.c
RU5P.p
X5P.p
R5P.p
EC2.p
F6P.p
E4P.p
S7P.p
SBP.p
G6P.p
6PG
Starch
ADPG
FBP.c
F6P.c
G6P.c
UDPG
Fructosyl
Glucosyl
Sucrose
PYR.c
ACA
ALA
CIT
ICI
AKG
SUC
FUM
MAL
OAA
PEP.c
ASP
ASN
THR
GLU
<1
1-10
10-40
40-160
>160

Integrated flux and pool size analysis in plant central metabolism reveals unique roles of glycine and serine during photorespiration

Authors: Xinyu Fu[1], Luke M. Gregory[1,2], Sean E. Weise[1], Berkley J. Walker[1,2]*

[1] Michigan State University-Department of Energy Plant Research Laboratory, Michigan State University, East Lansing, MI 48824, USA

[2] Department of Plant Biology, Michigan State University, East Lansing, MI 48824, USA

*Correspondence to: Berkley Walker, berkley@msu.edu

Abstract

Photorespiration is an essential process juxtaposed between plant carbon and nitrogen metabolism that responds to dynamic environments. Photorespiration recycles inhibitory intermediates arising from oxygenation reactions catalyzed by rubisco back into the C_3 cycle, but it is unclear what proportions of its nitrogen-containing intermediates (glycine and serine) are exported into other metabolisms *in vivo* and how these pool sizes affect net CO_2 gas exchange during photorespiratory transients. To address this uncertainty, we measured rates of amino acid export from photorespiration using isotopically nonstationary metabolic flux analysis. This analysis revealed that ~23-41% of the photorespiratory carbon was exported from the pathway as serine under various photorespiratory conditions. Furthermore, we determined that the build-up and relaxation of glycine pools constrained a large portion of photosynthetic acclimation during photorespiratory transients. These results reveal the unique and important roles of glycine and serine in successfully maintaining various photorespiratory fluxes that occur under environmental fluctuations in nature and providing carbon and nitrogen for metabolism.

Main

In C_3 plants, photorespiration is a high-flux metabolic pathway that recycles the inhibitory 2-phosphoglycolate (2PG) produced from the oxygenation reaction catalyzed by ribulose-1,5-bisphosphate carboxylase-oxygenase (rubisco). The recycling of 2PG to the C_3 intermediate, 3-phosphoglycerate (3PGA) involves a series of energy-consuming reactions across multiple organelles [1,2]. Upon cursory consideration, photorespiration is often viewed as a wasteful process, because the conversion from glycine to serine releases a large amount of CO_2 and ammonia, the former is released from photorespiration and the latter is re-assimilated with high-energy cost. However, besides the beneficial removal of 2PG, photorespiration also plays a vital role in central metabolism due to its close interaction with many other pathways, especially nitrate assimilation [3–6]. Although the interaction between photorespiration and nitrate assimilation is not mechanistically clear, nitrate assimilation depends to some degree on photorespiration [5,7]. For example, plants grown under elevated CO_2 partial pressures with decreased photorespiration have decreased nitrate assimilation into organic nitrogen (N) compounds and total N concentration of plant tissues [8,9]. Additionally, the major route of ammonia assimilation, glutamate synthesis, increases as photorespiration increases possibly not only facilitating increased rates of ammonia recapture from photorespiration but also increased rates of *de novo* nitrate assimilation [10,11].

The mechanism linking photorespiration to nitrate assimilation could be related to the export of N-rich amino acids from photorespiration. Due to the high metabolic flux channeled through photorespiration, even small changes in photorespiratory flux could affect the flux distribution through central carbon (C) and N metabolism. The extent to which photorespiration operates as a closed cycle to regenerate 3-PGA for the C_3 cycle or as an open cycle allowing metabolite export to interacting metabolisms remains unknown [12]. Exporting glycine and serine from photorespiration into non-photorespiratory metabolism (*e.g.,* protein synthesis, providing amino groups to alternative metabolic processes or transport) instead of returning their C to the chloroplast as 3PGA additionally affects the CO_2 loss and the energy costs associated with recycling of 2PG into 3PGA.

Evidence for a fraction of photorespiratory C exported from photorespiration as glycine and/or serine is revealed in biochemical modeling of leaf photosynthesis [13]. The export of photorespiratory C as amino acids can explain the decreased rates of net CO_2 assimilation (A) in response to CO_2 and O_2 at high CO_2 partial pressures, typically 2-4 times ambient conditions and saturating illumination [13]. In this paper we define glycine and serine export as amino acids that leave photorespiratory metabolism, this includes amino acids that leave the leaf entirely, as in phloem exudate, but also to amino acids that leave photorespiration to participate in non-photorespiratory metabolism in the same leaf tissue. The fraction of photorespiratory C exported as amino acids estimated using photosynthetic models ranges between 0.3-

0.77 under the high CO_2 partial pressures where this approach can be used, with serine being the primary amino acid exported [14,15]. Exporting glycine and serine from photorespiration increases photosynthesis at high CO_2 partial pressures when carbon assimilation is limited by the availability of inorganic phosphate in the chloroplast [16].

Exporting glycine and serine from photorespiration is also coupled to the N flux to these amino acids. Specifically, this N flux out of photorespiration in the form of amino acids must be supplemented by increasing the *de novo* assimilation of N to replace the amino groups required for glyoxylate amination to glycine, potentially explaining why the estimated fraction of amino acid export increases with increasing NO_3^- availability [15]. Despite this compelling evidence for serine and glycine export under high CO_2 partial pressures when photorespiration is limited, it is unclear if high rates of amino acid export happen under more physiologically relevant CO_2 partial pressures and forms a regular component of central metabolism under more typical growing conditions. C export from photorespiration also raises interesting questions concerning the functional importance of photorespiration, since this export would not replenish C lost from the C_3 cycle following rubisco oxygenation.

Another uncertainty of photorespiration is the speed of its metabolic response and subsequent impact on *A*. Photorespiration is a dynamic process, responding to *A*, stomatal conductance, and light regimes. However, it is mostly investigated under steady-state conditions by comparing the metabolomic profile and physiology following different environmental and genetic perturbations [17–19]. Under non-steady-state conditions, amounts of photorespiratory intermediates are sensitive to photorespiratory conditions both in the long- and short-term [17–19]. Photorespiratory intermediates additionally accumulate during transient changes in rubisco oxygenation rate or when downstream photorespiratory reactions are not stoichiometrically balanced [20–24]. When photorespiratory intermediates upstream of the glycine decarboxylase (GDC) reaction like glycine accumulate, the CO_2 release per rubisco oxygenation should decrease proportionally, increasing subsequent *A* during this accumulation. Despite this theoretical underpinning, it is not clear if the change in glycine pools is large enough to affect *A* to a measurable degree during transients in photorespiratory rates.

The use of isotopic tracers and metabolic flux analysis (MFA) are powerful tools to resolve how metabolism responds to environmental changes [25,26]. For example, isotopic labeling with $^{13}CO_2$ in combination with varied CO_2 and/or O_2 mole fraction has been commonly used to infer the impact of photorespiration on leaf C metabolism. Under different CO_2/O_2 conditions, distinct ^{13}C labeling enrichment has been observed in many primary and specialized metabolites [20,27], as well as proteins [28,29]. These studies were usually performed at isotopic pseudo-steady state with a single time-point, which does not allow flux quantification in autotrophic metabolism [30]. Recent development of isotopically

nonstationary metabolic flux analysis (INST-MFA) more fully leverages the benefits of $^{13}CO_2$ labeling to provide a global assessment of C fluxes through autotrophic leaf metabolism [26,31–34]. INST-MFA is therefore a promising approach for estimating fluxes and metabolic responses to changes in photorespiratory rates *in vivo*.

Here, INST-MFA was applied to examine the C fluxes through and out of the photorespiratory pathway under different photorespiratory conditions manipulated by the O_2 mole fraction. This INST-MFA analysis gave a quantitative estimate of serine and glycine exported from photorespiration under steady-state conditions at ambient CO_2 partial pressures, which agreed with estimates made under high CO_2 partial pressures using estimates from CO_2 response curves. Metabolite pool size measurements of 38 central metabolites showed that glycine had the strongest changes in response to photorespiratory shifts. We also determined that changes in glycine concentration were large enough to explain 20-30% of the gain in net CO_2 assimilation when transitioning from low to high photorespiratory conditions.

Results

Isotopically Nonstationary Metabolic Flux Analysis

To estimate C flux distribution on central metabolism, transient ^{13}C labeling experiments were performed on fully expanded *Nicotiana tabacum* (tobacco) leaves after short-term acclimation to three O_2 conditions (2%, 21%, and 40%). The labeling experiments were carried out at the same irradiance as the growth chamber (100 μmol m^{-2} s^{-1}) to minimize changes in metabolism due to light acclimation. Metabolic fluxes through central metabolism were determined from a metabolic network model (Supplementary Data 1), mass isotopologue distributions (MIDs) during the transient labeling period (Supplementary Data 2), and measured input and output fluxes to constrain the flux solutions. The independently determined input and output fluxes used to constrain the flux solution included the A, rubisco oxygenation rate (v_o), rubisco carboxylation rate (v_c), starch and sucrose production rates, and output flux ratios of amino acids and sucrose measured in vascular exudate (Supplementary Table 1 and 2 and Supplementary Method 1-4). INST-MFA was performed under the assumption that the metabolism is steady-state (Supplementary Method 4 with steady-state assumption validated below). The selection of labeling data for INST-MFA modeling and tests for several network models are described in Supplementary Method 4. A subset of key measured labeling data and the labeling kinetics simulated by the best-fit INST-MFA flux values are shown in Supplementary Figure 1 and the detailed fits of the best-fit models are shown in Supplementary Data 3.

Manipulating O_2 condition had a large and significant effect on v_o (2.60-26.37 μmol g^{-1} FW hr^{-1}) and a smaller but significant effect on v_c (53.36-79.70 μmol g^{-1} FW hr^{-1}, Fig. 1, 95% confidence intervals of the best-fit fluxes are shown in Supplementary Figure 2 and 3 and Supplementary Data 4). The rate of starch and sucrose synthesis decreased significantly with increasing rates of photorespiration (Fig. 1 and Supplementary Data 4). Direct measurement of the allocation of photo-assimilated C using $^{14}CO_2$ labelling showed that rates of starch and sucrose synthesis are strongly correlated with A (Supplementary Figure 4 and Supplementary Method 2).

The INST-MFA revealed the export rates of photorespiratory serine and glycine from the photorespiratory pathway at ambient CO_2 partial pressures (Fig. 1). The serine export rate to alternative sinks increased from 3.61 to 7.02 μmol g^{-1} FW hr^{-1} at high rates of photorespiration, but it decreased to 0.02 μmol g^{-1} FW hr^{-1} at low photorespiration rates. The export of glycine to alternative sinks was less than 0.01 μmol g^{-1} FW hr^{-1} at three conditions, much lower than that of serine. A portion of the export of amino acids from photorespiration, the removal of glycine or serine through phloem, was estimated based on the output flux to phloem and the output flux ratios of amino acids and sucrose measured in vascular exudate (Supplementary Table 2 and Supplementary Method 4). The removal rates of glycine or serine through the phloem were small relative to the total export, between 0.03 to 0.38 μmol g^{-1} FW hr^{-1} at various photorespiratory conditions (Fig. 1). The total amount of C leaving the photorespiratory pathway as serine scaled with the rate of photorespiration. At high photorespiration (40% O_2), 41% of the photorespiratory C influx (52.8 μmol C g^{-1} FW hr^{-1}) was exported as serine (at a rate of 21.5 μmol C g^{-1} FW hr^{-1}). The percentage of photorespiratory C leaving as serine was 32% at normal photorespiration (21% O_2) and 23% at low photorespiration (2% O_2). These data indicate that 23-41% of the photorespiratory C could be exported from the pathway as serine under physiologically relevant CO_2 partial pressures. The INST-MFA model was also run with glycerate labelling data and allowing glycerate export from the photorespiratory pathway. This extended model predicted that glycerate and glycine export rate was slow (< 0.1 μmol g^{-1} FW hr^{-1} in all oxygen conditions), while the serine export rate was slow at low photorespiration and rose at normal and high photorespiration (<0.1, 3.7 and 7.0 μmol g^{-1} FW hr^{-1} in 2%, 21%, and 40% O_2 respectively) (see Supplemental Method 4).

Estimating photorespiratory C export using CO_2 response of A

The export of photorespiratory C to amino acid synthesis or alternative metabolism accounts for the behavior of A at high CO_2 partial pressures in leaf photosynthesis models [13,15]. Using this approach, we estimated the fraction of C that leaves the photorespiratory pathway as glycine (α_G) and serine (α_S) using the measured CO_2 response of A at ambient O_2 and high light (~1000 μmol m^{-2} s^{-1}) fitted with the photosynthetic model over the triose phosphate utilization (TPU)-limited range to compare to the INST-

MFA results (Fig. 2). The high-CO_2 portion of the curve in orange, where TPU limits CO_2 assimilation, showed the characteristic curve that is only explained by amino acid removal from photorespiration [13,35]. This curvature was used to fit a resultant α_G and α_S of 0.01 and 0.45, indicating that the C flow out of photorespiration was primarily in the form of serine, consistent with the estimates ($\alpha_G < 0.01$ and $\alpha_S = 0.32$) calculated from the INST-MFA (Fig. 1).

Metabolic responses to low and high photorespiration

The absolute pool sizes of 38 central metabolic intermediates were measured in tobacco leaves exposed to varied photorespiratory conditions. Compared to the ambient O_2 condition, the metabolic changes at high photorespiration (40% O_2) and low photorespiration (2% O_2) were modest (Fig. 3). Most metabolites had insignificant changes in pool size during the short-term photorespiratory changes (Fig. 3 shows the mean fold-changes of the pool size between 2% and 21% O_2 or between 40% and 21% O_2; Supplementary Data 5 shows the absolute concentrations under the three oxygen conditions). The most significantly altered metabolites were photorespiratory intermediates (glycine, glycolate and glyoxylate), alanine, and ADPG (Supplementary Data 5). Many photorespiratory intermediates (glycine, serine, glycerate, glycolate and glyoxylate) were far from fully labelled even at high photorespiratory condition (Supplementary Figure 5). The average ^{13}C enrichment of these metabolites reached between 10% and 75% following 30 min of $^{13}CO_2$ labeling (Supplementary Figure 5), indicating that these intermediates exist in multiple subcellular pools with an active pool being involved in photorespiration and other pools (presumably in the vacuole [25]) not involved in photorespiration. The active and inactive pools of glycine were estimated using the measured total pool size and the dilution parameters from the INST-MFA (Supplementary Data 4 and 5). The extent of changes in glycine was much greater in the active pool (15-fold) than in the total pool (4-fold) (Fig. 4). These data support the steady-state assumption of INST-MFA (Supplementary Figure 6).

These data highlight the value of combining metabolite abundance with labeling and demonstrate the principle that in many cases changes in metabolite pool size do not directly translate into flux changes. For example, the pool size of 2PG was not significantly different between different oxygen conditions (Fig. 3 and Supplementary Data 5), but the ^{13}C labeling kinetics of 2PG were faster in high oxygen than in low oxygen (Supplementary Figure 1 and Supplementary Data 2), suggesting higher flux through rubisco oxygenation. This highlights that time-dependent labeling profiles are more informative indicators for flux rather than changes in pool sizes and that inferring flux from pool sizes alone can lead to inaccurate interpretations.

Photorespiration under non-steady state

Quantifying the steady-state active pool size of glycine at low and high photorespiratory conditions helped determine how much the size of glycine pools constrain net gas exchange during photorespiratory transients. To do this, *A* during O_2 transients was measured when tobacco leaves were exposed to 2% O_2 until the steady-state and then switched to 40% O_2. During the low-to-high O_2 transient, *A* did not instantly reach a new steady state at 40% O_2 but gradually declined at an exponential rate for ~2 min until the new steady-state was reached (Fig. 5). The extra C gained or lost during the transient in the decrease (or increase) in *A* as compared to how much C would be fixed with an instant transition to the new steady state was defined as the "C lag", which can be quantified by integrating the area between the fitted curve of *A* and a baseline of *A* at the new steady state (Fig. 5a). During the transition from 2% O_2 to 40% O_2, the total glycine pool increased by 30.8 ± 2.4 μmol m^{-2} based on the differences in steady-state levels (after 30 min acclimation to high or low oxygen) between high and low oxygen levels (Fig 4) or 20.8 ± 6.2 μmol m^{-2} based on the initial build-up of glycine pool after switching oxygen for 60 s when the gas exchange transient is near complete (Supplementary Figure 7), accounting for 20-30% of the total C lag (50.4 ± 1.7 μmol m^{-2}) as the accumulated glycine would otherwise be metabolized by the downstream glycine decarboxylase reaction (2 mol of glycine yielding 1 mol of CO_2). The build-up of the active glycine pool based on the steady-state measurement (25.7 ± 3.4 μmol m^{-2}, Fig 4) accounted for ~25% of the total C lag. When looking at the transition from 40% O_2 to 2% O_2, the lag in the photosynthetic increase resulted in loss of C represented by the shaded area (Fig. 5b). The reduction of the active glycine pool based on the steady-state measurement explained ~15% of this total C lag (83.9 ± 3.8 μmol m^{-2}). Note that the change in concentrations in response to O_2 treatment is negligible and small in other metabolites upstream of glycine (i.e. 2PG, glycolate and glyoxylate, Fig. 5), further indicating glycine is the primary metabolic pool impacting this transient response.

Discussion

Impact of photorespiratory flux changes on C and N metabolism

Our INST-MFA indicates that C was exported from photorespiration under ambient CO_2 partial pressures as serine at high rates. The INST-MFA-estimated fraction of serine export is 0.27-0.39 (95% confidence interval using the parameter continuation method) under ambient O_2 and CO_2 partial pressures (Supplementary Figure 2 and Supplementary Data 4), which is close to the 95% confidence interval of the value estimated using photosynthetic models fitted at high CO_2 partial pressures (0.38-0.51) (Fig. 2). Given these large export rates, where do these amino acids go? Prior studies have shown that glycine is incorporated into leaf protein when photorespiration is induced by low CO_2 [28,36], and almost all

photorespiratory glycine is routed to protein synthesis in water-stressed soybean leaves under high light and low CO_2 partial pressure [29]. Protein synthesis is not likely to explain all the amino acid export from photorespiration, since glycine and serine are present in similar proportions in total plant protein, but serine is exported at a much higher rate [37]. Past work also suggests that at least some photorespiratory serine and glycine is exported out of source leaves under photorespiratory conditions as is evident by an increased labeling in serine and glycine within the petiole when source leaves were labeled with $^{14}CO_2$ under elevated O_2 [38], but our vascular exudates indicated that removal from the leaf only accounted for a small percentage of the total amino acids exported from photorespiration. Photorespiratory glycine and serine are also required for the synthesis of various essential metabolites. For example. serine provides the carbon backbone for the synthesis of cysteine and tryptophan, which are further used to produce sulphur-containing compounds (*e.g.* S-adenosylmethionine) and indolic compounds (*e.g.* auxin and glucosinolates) [39,40]. Serine also is an important substrate for the biosynthesis of phosphatidylserine and sphingolipid that are critical to plant development and survival [41]. Glycine enhances the synthesis of glutathione (γ-Glu–Cys–Gly) as suggested by previous leaf feeding experiments [42]. Taken together, these findings indicate that photorespiration is an important source of amino acids for protein and metabolite synthesis and future work should work to resolve where specifically this serine goes within metabolism.

The increased fraction of photorespiratory C exported as amino acids with increased photorespiration in this study also helps explain the mechanistic link between photorespiration and N metabolism [5,43]. Large serine export fluxes diverted from photorespiration would need to be supplemented by equivalent *de novo* N assimilation. The *de novo* N assimilation rate would need to increase to support a higher total amount of photorespiratory C leaving as amino acids under higher photorespiratory condition. Supporting this hypothesis, plants under ambient photorespiration had ~10-30% higher N assimilation rates than those under low photorespiration (high CO_2 or low O_2) [8]. The coupling of N assimilation with photorespiration-derived glycine and serine has also been suggested from a dual labeling study with $^{13}CO_2$ and ^{15}N-ammonium nitrate [44]. In this 6-h labeling study, up to 50% of ^{15}N glycine and ^{15}N serine molecules were also ^{13}C enriched, probably due to large turnover glycine and serine associated with high flux rates of photorespiration, whereas many other amino acids were only ^{15}N-labelled because their ^{15}N-amino groups were not fixed onto ^{13}C-enriched C skeletons. Exporting glycine and serine from the photorespiratory pathway could enable plants to efficiently assimilate N onto C skeletons produced during photorespiration, also stimulating CO_2 uptake at high CO_2 [15].

The finding that large amounts of C leave photorespiration for other metabolisms and do not re-enter the C_3 cycle suggests some interesting hypotheses concerning the central purpose of photorespiration. Photorespiration is thought to be essential for returning C back into the C_3 cycle, but our flux values

indicate that only 43% returns following serine export, instead of the theoretically maximal 75% under 21% O_2. This rate of carbon removal is (large) relative to other fluxes in central metabolism, comprising 50% and 62% the C flux of starch and sucrose syntheses at 21% O_2. This indicates that the C_3 cycle is resilient against carbon removal and can replenish its own intermediates even under high rates of removal following rubisco oxygenation. This is not surprising given the ability for the C_3 cycle to operate even under high rates of rubisco oxygenation, like what occurs under 40% O_2 or elevated temperatures. Conceptually this is similar to carbon removal from the C3 cycle to other metabolisms like sucrose and starch. These findings favor the hypothesis that the major roles of photorespiration are to provide C and N for downstream metabolism in addition to processing inhibitory byproducts of rubisco oxygenation. This would help explain why it interacts with so many other aspects of metabolism. It may also explain why photorespiration is maintained in all oxygenic phototrophs, and is even essential (albeit in reduced amounts) in plant species with an efficient carbon concentrating mechanism in addition to its role in processing 2PG [45].

Role of glycine in photorespiration and *A* during transients

Our metabolomics analyses identified a significant correlation between photorespiratory rate and glycine pool size, which is large enough to explain much of the transient response of *A* to changing photorespiratory conditions. The metabolically active glycine pools inferred from the dilution parameters in our INST-MFA changed 15-fold when comparing low and high photorespiration (Fig. 4). Our gas exchange data showed that during the low-to-high O_2 transient, the concomitant accumulation of active glycine pools that are not decarboxylated accounted for ~25% of the excess CO_2 fixed (Fig. 5a). Interestingly, the relaxation of active glycine pools accounts for a slightly smaller ~15% of the excess CO_2 lost during the high-low O_2 transient (Fig. 5b). These findings indicate a unique connection between the accumulation of a single metabolite and the subsequent effects to *A*. Further research is needed to determine what the remaining determinants of the acclimation of net assimilation between photorespiratory conditions are and how well these findings translate to other changes in photorespiratory rate, like under fluctuating light [46].

These findings support a hypothesis as to the role of glycine in photorespiration as a “safe” buffering metabolite in a dynamic pathway. The biochemical structure and kinetics of photorespiration may be configured to accumulate glycine so that other upstream or downstream intermediates do not change too rapidly or build up to inhibitory or cytotoxic concentrations. Photorespiratory intermediates downstream of glycine were not significantly changed at varying photorespiratory conditions (Fig. 3). Many other

studies have shown that glycine is the most drastically changed photorespiratory intermediates upon photorespiratory pressures [17,18,20,21,47], suggesting that glycine is a well-tolerated metabolite in plant cells. The build-up of glycine may also suggest that photorespiration has been optimized to delay the release of ammonium until there is sufficient glutamine synthetase/glutamate synthase activity to recapture the ammonium released from the GDC reaction. In contrast, other photorespiratory intermediates are riskier to accumulate. For example, the cytotoxicity of 2-PG, glycolate, glyoxylate, and serine suggests tight regulation of their intracellular concentrations [45,48–52]. The toxicity of glycolate and glyoxylate may be more nuanced however, since transformants expressing novel photorespiratory genes had ~3 and ~8 fold higher concentrations of glycolate and glyoxylate with no obvious cytotoxic effects [53]. In addition to these cytotoxic intermediates, serine may act as a signal for the transcriptional regulation of photorespiration-related genes, as external supply of serine induces transcriptional deregulation so pool sizes would need to be relatively buffered to prevent a hyper-sensitivity to short-term changes in photorespiratory flux [54]. Furthermore, accumulated glycerate could exert a feed-back effect on photosynthesis by blocking the stromal fructose-1,6-bisphosphatase [55]. Of all the photorespiratory intermediates, glycine therefore appears to be the most inert to metabolism and therefore a waypoint to help safely navigate dynamic changes in flux.

The transient build-up in glycine pools when switching from low to high photorespiratory condition indicates that the capacity of the downstream photorespiratory enzyme GDC may not be sufficient to process large changes in glycine influx under non-steady state conditions. Limiting GDC activity even by ~50% leads to a 100-fold accumulation of glycine during the day, while stimulating GDC activity leads to a ~40% reduction in steady-state level of glycine [56,57]. Moreover, upregulating GDC activity improves plant performance both in the laboratory and field conditions [57,58], suggesting its key role in controlling photorespiratory flux. While GDC is normally not limited by its substrate glycine and NAD^+, the efficient operation of GDC requires maintaining low levels of its product NADH, which may accumulate during rapid changes in flux through GDC [59]. The mitochondrial TRX system has been proposed to be important in the redox regulation of GDC under fluctuating light, adding to its potential role under transient conditions[60,61].

An additional explanation for the increase in glycine pools relative to serine during increasing photorespiration is the need to maintain appropriate concentration gradients to drive transport of these metabolites between the mitochondrion and peroxisome. While these transporters are not yet identified, they must facilitate large fluxes and are most likely driven by concentration gradients that are proportional to their fluxes [62]. Glycine flux into the mitochondria is twice as large as serine flux out since the GDC/serine hydroxymethyltransferase reactions require two glycine per serine produced and

assuming a "closed cycle" of photorespiration. Since higher transport gradients would translate to higher leaf-level pool sizes of metabolites, the differences in flux may also help explain the high build-up of glycine relative to serine.

Methods

Plant material. Tobacco (*Nicotiana tabacum*) plants were grown in a growth chamber under an 18-h day/6-h night photoperiod at a light intensity of 100 μmol m^{-2} s^{-1}, day/night temperatures of 23°C/18°C, and relative humidity of 60%. All experiments were performed on the fully expanded source leaves of 8-week-old plants.

Gas exchange and $^{13}CO_2$ labeling system. Leaf gas exchange measurements under controlled $O_2/CO_2/N_2$ conditions were performed using a LI-6800 (LI-COR Biosciences, USA) with a fast atmospheric switching and quenching system as described previously [33]. Leaves were equilibrated and monitored in the cuvette at 40 Pa $^{12}CO_2$ levels with three O_2/N_2 conditions (2% O_2 / 98% N_2, 21% O_2/ 79% N_2, and 40% O_2/ 60 % N_2), light intensity of 100 μmol photon m^{-2} s^{-1}, leaf temperature of 25 °C, and relative humidity of 70%. $^{13}CO_2$ labeling was performed after 20-30 min of acclimation to reach a photosynthetic steady-state. Illuminated leaves were incubated at 0, 0.5, 1, 2, 2.5, 3, 5, 7, 10, 15, and 30 min with $^{13}CO_2$-containing gas mixture ([40 Pa] $^{13}CO_2$ with each O_2/N_2 condition) before quenching. Pseudo-steady state metabolism was assumed during the labeling period at each oxygen condition (Supplementary Figure 6). Detailed descriptions of tissue harvesting and quenching for metabolic analyses are shown in Supplementary Method 1.

Metabolite labeling and concentration. The extraction and analytical procedures for quantifying metabolite labeling and concentration were similar to the method described previously [33]. Gas chromatography-mass spectrometry (GC-MS) was used to analyze amino acids, organic acids, and sugars. Ion-pair chromatography-tandem mass spectrometry (IPC-MS/MS) was used to analyze the phosphorylated intermediates in C_3 cycle. Anion exchange chromatography-tandem mass spectrometry (AEC-MS/MS) was used to analyze nucleotide sugars and additional phosphorylated intermediates. Detailed descriptions of the extraction and mass spectrometry analyses are shown in Supplementary Method 1 and Supplementary Data 6. Abbreviations of metabolites are shown in Supplementary Data 7.

Measurements of external fluxes. Rates of starch and sucrose synthesis were measured by the steady state pulse-chase labeling of $^{14}CO_2$ as described previously [35] with slight modifications (Supplementary Method 2). Rates of rubisco carboxylation and oxygenation were calculated as described earlier using gas

exchange measurements [2], with the required biochemical and diffusional parameters experimentally estimated by gas exchange and isotope analysis (see Supplementary Method 3 for details). The output flux ratios of amino acids and sucrose were estimated by measuring steady-state levels of sucrose and amino acids in vascular exudate as described earlier [26,33]. Detailed descriptions of exudate collection were described in Supplementary Method 1.

Metabolic network and flux determination. The network model used for flux determination was modified from published reaction models [26,33,34] (Supplementary Data 1). INST-MFA was performed using the elementary metabolite unit (EMU)-based software INCA (version 1.8) [63] ran within MATLAB 2018b (Mathworks, USA). Model formulation details are described in Supplementary Method 4 and the INCA model files are included in Supplementary Data 8. Metabolic fluxes were estimated by iteratively minimizing the sum of squared residuals (SSR) between the experimentally measured and simulated isotopic labeling patterns and measured external rates, using a Levenberg-Marquardt optimization algorithm [64]. Each flux estimation was repeated a minimum of 100 times from random initial values to find best-fit estimates. All results were subjected to a χ^2-statistical test for goodness-of-fit and the 95% confidence intervals were computed for all estimated fluxes using two independent methods. A parameter continuation method was used to evaluate the sensitivity of SSR to flux variations [65]. A Monte Carlo method was used to estimate flux distributions based on 3,000 sets of external flux measurements and MID data perturbed by normally distributed noise with the measured SD. The parameter continuation and Monte Carlo simulations were computed in parallel using a high-performance computing environment (Institute for Cyber-Enabled Research at Michigan State University) and a cloud computing environment (Microsoft Azure). The cloud-based workflow to run the Monte Carlo simulations can be found at https://github.com/codexf/MFA_Cloud_Computing.

Estimating photorespiratory C export using CO_2 response of *A*. A/C_c curves were measured with a LI-6800 at a light intensity of 1000 μmol photon m^{-2} s^{-1} and a leaf temperature of 25 °C. The sequence of reference CO_2 partial pressures was 40, 5, 7.5, 10, 15, 20, 25, 30, 35, 40, 45, 50, 60, 80, 100, and 120 Pa. Photosynthetic parameters, including the C exported from photorespiration as glycine (α_G) or serine (α_S), were estimated from the A/C_i curves using the modified Farquhar, von Caemmerer and Berry (FvCB) biochemical model of photosynthesis fitted against rubisco, RuBP-regeneration, triose-phosphate use limitations, α_G and (α_S) [15,66,67]. Data and custom scripts can be found at https://github.com/codexf/Modeling_Photosynthesis.

Transient response of *A* to changes in O_2 mole fraction. Dynamic photosynthesis was recorded using a LI-6800 with 2-s intervals. The leaves were illuminated (100 μmol m^{-2} s^{-1}) in 40 Pa CO_2 levels (CO_2 injector manually controlled) with either high O_2 (40% O_2 / 60% N_2) or low O_2 (2% O_2 / 98% N_2). When

the steady-state rate of *A* had been achieved, the cuvette was switched to low or high O_2 and leaves were left to reach a new steady-state rate of *A*. The time course data were fitted using one-phase exponential functions and the integrated area between the fitted curve and the baseline of the new steady-state *A* was calculated to estimate the total C lag during the transients. Data and custom scripts can be found at https://github.com/codexf/Modeling_Photosynthesis.

Data availability

All data used in this study are provided as Supporting Information of the article or available upon request. Gas exchange data for modeling the photosynthetic responses to carbon dioxide concentration and photosynthetic responses during oxygen transients can be found on GitHub at https://github.com/codexf/Modeling_Photosynthesis.

Code availability

Custom scripts for modeling the photosynthetic responses to carbon dioxide concentration and photosynthetic responses during oxygen transients can be found on GitHub at https://github.com/codexf/Modeling_Photosynthesis. A cloud-based workflow to run the Monte Carlo simulations for computing confidence intervals of metabolic fluxes can be found on GitHub at https://github.com/codexf/MFA_Cloud_Computing.

Acknowledgements

We thank Aikaari Ryce at Michigan State University (MSU) for experimental assistance; Thomas D. Sharkey (MSU) for providing lab space and guidance for performing the $^{14}CO_2$ labeling experiments; Yuan Xu and Yair Shachar-Hill (MSU) for helpful discussions on INST-MFA; James Klug and Cody Keilen (MSU Growth Chamber Facility) for plant maintenance; A. Daniel Jones, Lijun Chen, and Casey Johnny (MSU Mass Spectrometry and Metabolomics Core Facility) for advising metabolomics analyses; Patrick Bills (MSU IT Services), Xiaoge Wang, and Mahmoud Parvizi (MSU Institute for Cyber-Enabled Research) for consulting on cloud computing and high-performance computing. The computational work was supported in part through the high-performance computing cluster and services provided by the Institute for Cyber-Enabled Research at MSU. The computational work was also supported in part through MSU's Institute for Cyber-Enabled Research Cloud Computing Fellowship, with computational

resources and services provided by Information Technology Services and the Office of Research and Innovation at MSU. We also thank Jamey Young for making INCA accessible and Hilary Stewart Williams for help establishing the online isotope analysis system. This work was supported by the U.S. Department of Energy Office of Science, Basic Energy Sciences under Award DE- FG02-91ER20021 (BJW, XF, and SEW). This material is also based upon work supported in part by the Great Lakes Bioenergy Research Center, U.S. Department of Energy, Office of Science, Office of Biological and Environmental Research under Award Number DE-SC0018409 (BJW) and the National Science Foundation under Grant No. 2030337 (BJW and LMG). We also thank the constructive feedback from three anonymous reviewers, which greatly increased the quality and strength of this work.

Author contributions

BJW and XF designed the experiments. XF carried out the bulk of the experiments and analyzed the results. SEW advised and assisted the $^{14}CO_2$ experiments to measure starch and sucrose partitioning. LG performed the isotope analysis to measure gas exchange parameters. XF wrote the manuscript with contributions from all the authors. BJW serves as the author responsible for contact and ensures communication.

Competing interests

The authors declare no competing interests.

Figure legends

Fig. 1: Central carbon assimilatory metabolic fluxes in tobacco leaves exposed to varying O_2 conditions. Fluxes were estimated by ^{13}C INST-MFA using the metabolic network model and experimental inputs including mass isotopologue distributions of measured metabolites, the net CO_2 assimilation rate, rates of rubisco carboxylation and oxygenation, rates of starch and sucrose synthesis, and output flux ratios of amino acids and sucrose. Best-fit flux estimates are shown in numbers and corresponding variable width of arrows. Arrows in blue indicate reactions constrained (not fixed) based on the experimental measurements (Supplementary Table 1). Flux units are expressed as μmol molecule g^{-1} FW hr^{-1} (for the conversion to μmol carbon g^{-1} FW hr^{-1}, multiply the presented values by the number of carbons in the molecule). Metabolites compartmentalized to the plastid and cytosol are denoted by (".p") and (".c") respectively. Abbreviations are shown in Supplementary Data 7.

Fig. 2: The response of A to the chloroplastic CO_2 concentration (Cc) in tobacco leaves exposed to 21% O_2 under high light (1000 μmol m^{-2} s^{-1}). Measured A are presented as dots with error bars (mean ± SD, n = 9 biologically independent leaves) fitted with the modified Farquhar, von Caemmerer and Berry (FvCB) biochemical model of photosynthesis with two terms α_G and α_S, where α_G is the proportion of the carbon exported from the photorespiratory pathway as glycine, and α_S the proportion of the carbon exported from photorespiration as serine (see Method section: *Estimating photorespiratory C export using CO_2 response of A*). The parameter values obtained from the individual fits are shown as mean ± SD (n = 9 biologically independent leaves), including the maximum rubisco carboxylation rate (V_{cmax}), the maximum rate of electron transport (J), the rate of triose phosphate export from the chloroplast (T_p), α_G and α_S. The curves represent Rubisco (red), RuBP (green), and TPU (orange) limitation.

Fig. 3: Metabolic pool size alterations in response to photorespiratory conditions. Tobacco leaves were exposed to the three O_2/N_2 conditions (all at 40 Pa $^{12}CO_2$ levels) in the LI-6800 cuvette for 30 min until quenching with liquid nitrogen under illumination. Leaves acclimated to 2% O_2 and 40% O_2 were compared to the ambient O_2 condition respectively and the steady-state pool sizes of the identified metabolites (plotted on the y-axis) were determined using GC-MS and LC-MS/MS. The x-axis plots the log2-transformed relative ratio of abundance of each metabolite in the leaves exposed to 2% O_2 (blue) or 40% O_2 (red) normalized to the same metabolite in the leaves exposed to 21% O_2. Results are presented as dots with error bars (mean ± SEM, n = 7 or 8 biologically independent leaves). Asterisk represents a significant difference between two conditions (Benjamini-Hochberg procedure was used to control the false discovery rate at 0.05 for multiple *t*-tests including all metabolites). Supplementary Data 5 presents the absolute concentration of each metabolite under different oxygen conditions with the results of one-way ANOVA followed by Tukey's test for multiple pairwise comparisons among the three oxygen conditions per metabolite. Abbreviations of metabolites are shown in Supplementary Data 7.

Fig. 4: Active and inactive pools of glycine at varying O_2 levels. Tobacco leaves were exposed to the three O_2/N_2 conditions (all at 40 Pa $^{12}CO_2$ levels) in the LI-6800 cuvette for 30 min until quenching with liquid nitrogen under illumination. Steady-state pool sizes of glycine were determined using GC-MS. The proportion of active (gray) and inactive (white) pools of glycine were estimated using the dilution parameters in INST-MFA modeling. Data are presented as box plots (center line at the median, upper bound at 75th percentile, lower bound at 25th percentile) with whiskers extended to the extreme data point ≤ 1.5 × interquartile range from the edge of the box (n = 7 or 8 biologically independent leaves). Different letters above the data boxes denote statistically significant differences among the three conditions for active glycine pools (uppercase letters) and inactive glycine pools (lowercase letters) at $P <$ 0.05 (one-way ANOVA followed by Tukey's test for multiple pairwise comparisons). For active glycine

pools, the P values for Tukey multiple comparisons of means are 0.0006 (2% O2 - 21% O2), <0.0001 (2% O2 - 40% O2), and 0.0042 (21% O2 - 40% O2). For inactive glycine pools, the P values for Tukey multiple comparisons of means are 0.0260 (2% O2 - 21% O2), 0.0138 (2% O2 - 40% O2), and 0.9511 (21% O2 - 40% O2).

Fig. 5: Dynamics of net CO_2 assimilation rate (A) during oxygen transients from 2% O_2 to 40% O_2 (a) and from 40% O_2 to 2% O_2 (b). The leaves were acclimated in a LI-6800 cuvette at low O_2 or high O_2 for 30 min to reach the photosynthetic steady-state. Upon switching to the opposite oxygen condition, A changed drastically due to slow gas mixing and returned to the previous steady state within ~10 s. The time when the previous steady state was reached after switching oxygen was set to zero for the convenience of curve fitting. Data points of different colors correspond to independent time-course measurements on ten different plants. Lines of different colors represent the fitted curves of a one-phase exponential function for individual replicates. Integrated area between the fitted curve and the baseline of new steady state for a represented replicate is presented in the inserts. The integrated area obtained from the ten individual fits are shown as mean ± SD (n = 10 biologically independent leaves).

References

1. Walker, B. J., Kramer, D. M., Fisher, N. & Fu, X. Flexibility in the energy balancing network of photosynthesis enables safe operation under changing environmental conditions. *Plants* **9**, (2020).
2. Bauwe, H., Hagemann, M. & Fernie, A. R. Photorespiration: players, partners and origin. *Trends Plant Sci.* **15**, 330–336 (2010).
3. Bauwe, H., Hagemann, M., Kern, R. & Timm, S. Photorespiration has a dual origin and manifold links to central metabolism. *Curr. Opin. Plant Biol.* **15**, 269–275 (2012).
4. Hanson, A. D. & Roje, S. One-carbon metabolism in higher plants. *Annu. Rev. Plant Biol.* **52**, 119–137 (2001).
5. Bloom, A. J. Photorespiration and nitrate assimilation: A major intersection between plant carbon and nitrogen. *Photosynth. Res.* **123**, 117–128 (2015).
6. Tcherkez, G. *et al.* Respiratory metabolism of illuminated leaves depends on CO2 and O2 conditions. *Proc. Natl. Acad. Sci. U. S. A.* **105**, 797–802 (2008).
7. Rachmilevitch, S., Cousins, A. B. & Bloom, A. J. Nitrate assimilation in plant shoots depends on photorespiration. *Proc. Natl. Acad. Sci. U. S. A.* **101**, 11506–11510 (2004).
8. Bloom, A. J., Burger, M., Asensio, J. S. R. & Cousins, A. B. Carbon dioxide enrichment inhibits nitrate assimilation in wheat and arabidopsis. *Science (80-.).* **328**, 899–903 (2010).
9. Cotrufo, M. F., Ineson, P. & Scott, A. Elevated CO2 reduces the nitrogen concentration of plant tissues. *Glob. Chang. Biol.* **4**, 43–54 (1998).
10. Abadie, C., Blanchet, S., Carroll, A. & Tcherkez, G. Metabolomics analysis of postphotosynthetic effects of gaseous O2 on primary metabolism in illuminated leaves. *Funct. Plant Biol.* **44**, 929–940 (2017).
11. Tcherkez, G. *et al.* Short-term effects of CO2 and O2 on citrate metabolism in illuminated leaves. *Plant, Cell Environ.* **35**, 2208–2220 (2012).
12. Hodges, M. *et al.* Perspectives for a better understanding of the metabolic integration of photorespiration within a complex plant primary metabolism network. *Journal of Experimental*

Botany vol. 67 3015–3026 (2016).
13. Harley, P. C. & Sharkey, T. D. An improved model of C3 photosynthesis at high CO2: Reversed O2 sensitivity explained by lack of glycerate reentry into the chloroplast. *Photosynth. Res.* **27**, 169–178 (1991).
14. Busch, F. A. & Sage, R. F. The sensitivity of photosynthesis to O2 and CO2 concentration identifies strong Rubisco control above the thermal optimum. *New Phytol.* **213**, 1036–1051 (2017).
15. Busch, F. A., Sage, R. F. & Farquhar, G. D. Plants increase CO2 uptake by assimilating nitrogen via the photorespiratory pathway. *Nat. Plants* **4**, 46–54 (2018).
16. McClain, A. M. & Sharkey, T. D. Triose phosphate utilization and beyond: From photosynthesis to end product synthesis. *J. Exp. Bot.* **70**, 1755–1766 (2019).
17. Eisenhut, M. *et al.* Photorespiration is crucial for dynamic response of photosynthetic metabolism and stomatal movement to altered CO2 availability. *Mol. Plant* **10**, 47–61 (2017).
18. Timm, S. *et al.* High-to-low CO2 acclimation reveals plasticity of the photorespiratory pathway and indicates regulatory links to cellular metabolism of Arabidopsis. *PLoS One* **7**, e42809 (2012).
19. Wingler, A. *et al.* The role of photorespiration during drought stress: An analysis utilizing barley mutants with reduced activities of photorespiratory enzymes. *Plant, Cell Environ.* **22**, 361–373 (1999).
20. Abadie, C., Bathellier, C. & Tcherkez, G. Carbon allocation to major metabolites in illuminated leaves is not just proportional to photosynthesis when gaseous conditions (CO2 and O2) vary. *New Phytol.* **218**, 94–106 (2018).
21. Abadie, C., Boex-Fontvieille, E. R. A., Carroll, A. J. & Tcherkez, G. In vivo stoichiometry of photorespiratory metabolism. *Nat. plants* **2**, 15220 (2016).
22. Abadie, C. & Tcherkez, G. 13C isotope labelling to follow the flux of photorespiratory intermediates. *Plants* **10**, 1–12 (2021).
23. Bao, H. *et al.* Catalase protects against nonenzymatic decarboxylations during photorespiration in Arabidopsis thaliana. *Plant Direct* **5**, (2021).
24. Tcherkez, G. *et al.* Leaf day respiration: low CO2 flux but high significance for metabolism and carbon balance. *New Phytol.* **216**, 986–1001 (2017).
25. Szecowka, M. *et al.* Metabolic fluxes in an illuminated Arabidopsis rosette. *Plant Cell* **25**, 694–714 (2013).
26. Ma, F., Jazmin, L. J., Young, J. D. & Allen, D. K. Isotopically nonstationary 13C flux analysis of changes in Arabidopsis thaliana leaf metabolism due to high light acclimation. *Proc. Natl. Acad. Sci. U. S. A.* **111**, 16967–16972 (2014).
27. Abadie, C., Lalande, J., Limami, A. M. & Tcherkez, G. Non-targeted 13C metabolite analysis demonstrates broad re-orchestration of leaf metabolism when gas exchange conditions vary. *Plant Cell Environ.* **44**, 445–457 (2021).
28. Cegelski, L. & Schaefer, J. NMR determination of photorespiration in intact leaves using in vivo 13CO2 labeling. *J. Magn. Reson.* **178**, 1–10 (2006).
29. Dirks, R. C., Singh, M., Potter, G. S., Sobotka, L. G. & Schaefer, J. Carbon partitioning in soybean (Glycine max) leaves by combined 11C and 13C labeling. *New Phytol.* **196**, 1109–1121 (2012).
30. Ratcliffe, R. G. & Shachar-Hill, Y. Measuring multiple fluxes through plant metabolic networks. *Plant J.* **45**, 490–511 (2006).
31. Chu, K. L. *et al.* Metabolic flux analysis of the non-transitory starch tradeoff for lipid production in mature tobacco leaves. *Metab. Eng.* **69**, 231–248 (2022).
32. Treves, H. *et al.* Carbon flux through photosynthesis and central carbon metabolism show distinct patterns between algae, C3 and C4 plants. *Nat. Plants* **8**, 78–91 (2022).
33. Xu, Y., Fu, X., Sharkey, T. D., Shachar-Hill, Y. & Walker, B. J. The metabolic origins of non-photorespiratory CO2 release during photosynthesis: A metabolic flux analysis. *Plant Physiol.*

186, 297–314 (2021).
34. Xu, Y., Wieloch, T., Kaste, J. A. M., Shachar-Hill, Y. & Sharkey, T. D. Reimport of carbon from cytosolic and vacuolar sugar pools into the Calvin-Benson cycle explains photosynthesis labeling anomalies. *Proc. Natl. Acad. Sci. U. S. A.* **119**, (2022).
35. Sharkey, T. D., Berry, J. A. & Raschke, K. Starch and sucrose synthesis in Phaseolus vulgaris as affected by light, CO2, and abscisic acid. *Plant Physiol.* **77**, 617–620 (1985).
36. Cegelski, L. & Schaefer, J. Glycine metabolism in intact leaves by in vivo13C and 15N labeling. *J. Biol. Chem.* **280**, 39238–39245 (2005).
37. Heinemann, B., Künzler, P., Eubel, H., Braun, H. P. & Hildebrandt, T. M. Estimating the number of protein molecules in a plant cell: protein and amino acid homeostasis during drought. *Plant Physiol.* **185**, 385–404 (2021).
38. Madore, M. & Grodzinski, B. Effect of oxygen concentration on 14C-photoassimilate transport from leaves of Salvia splendens L. *Plant Physiol.* **76**, 782–786 (1984).
39. Takahashi, H., Kopriva, S., Giordano, M., Saito, K. & Hell, R. Sulfur assimilation in photosynthetic organisms: Molecular functions and regulations of transporters and assimilatory enzymes. *Annu. Rev. Plant Biol.* **62**, 157–184 (2011).
40. Radwanski, E. R. & Last, R. L. Tryptophan biosynthesis and metabolism: Biochemical and molecular genetics. *Plant Cell* **7**, 921–934 (1995).
41. Ros, R., Muñoz-Bertomeu, J. & Krueger, S. Serine in plants: Biosynthesis, metabolism, and functions. *Trends Plant Sci.* **19**, 564–569 (2014).
42. Noctor, G., Arisi, A. C. M., Jouanin, L. & Foyer, C. H. Photorespiratory glycine enhances glutathione accumulation in both the chloroplastic and cytosolic compartments. *J. Exp. Bot.* **50**, 1157–1167 (1999).
43. Foyer, C. H., Bloom, A. J., Queval, G. & Noctor, G. Photorespiratory metabolism: Genes, mutants, energetics, and redox signaling. *Annu. Rev. Plant Biol.* **60**, 455–484 (2009).
44. Gauthier, P. P. G. *et al.* In folio isotopic tracing demonstrates that nitrogen assimilation into glutamate is mostly independent from current CO2 assimilation in illuminated leaves of Brassica napus. *New Phytol.* **185**, 988–999 (2010).
45. Zelitch, I., Schultes, N. P., Peterson, R. B., Brown, P. & Brutnell, T. P. High glycolate oxidase activity is required for survival of maize in normal air. *Plant Physiol.* **149**, 195–204 (2009).
46. Fu, X. & Walker, B. J. Dynamic response of photorespiration in fluctuating light environments. *J. Exp. Bot.* (2022) doi:https://doi.org/10.1093/jxb/erac335.
47. Hitz, W. D. & Stewart, C. R. Oxygen and carbon dioxide effects on the pool size of some photosynthetic and photorespiratory intermediates in soybean (Glycine max [L.] Merr.). *Plant Physiol.* **65**, 442–446 (1980).
48. Flügel, F. *et al.* The photorespiratory metabolite 2-phosphoglycolate regulates photosynthesis and starch accumulation in Arabidopsis. *Plant Cell* **29**, 2537–2551 (2017).
49. Anderson, L. E. Chloroplast and cytoplasmic enzymes II. Pea leaf triose phosphate isomerases. *BBA - Enzymol.* **235**, 237–244 (1971).
50. Campbell, W. J. & Ogren, W. L. Glyoxylate inhibition of ribulosebisphosphate carboxylase/oxygenase activation in intact, lysed, and reconstituted chloroplasts. *Photosynth. Res.* **23**, 257–268 (1990).
51. Gonzalez-Moro, B., Lacuesta, M., Becerril, J. M., Gonzalez-Murua, C. & Munoz-Rueda, A. Glycolate accumulation causes a decrease of photosynthesis by inhibiting RUBISCO activity in maize. *J. Plant Physiol.* **150**, 388–394 (1997).
52. Kelly, G. J. & Latzko, E. Inhibition of spinach-leaf phosphofructokinase by 2-phosphoglycollate. *FEBS Lett.* **68**, 55–58 (1976).
53. South, P. F., Cavanagh, A. P., Liu, H. W. & Ort, D. R. Synthetic glycolate metabolism pathways

stimulate crop growth and productivity in the field. *Science (80-.).* **363**, (2019).
54. Timm, S. *et al.* Serine acts as a metabolic signal for the transcriptional control of photorespiration-related genes in Arabidopsis. *Plant Physiol.* **162**, 379–389 (2013).
55. Schimkat, D., Heineke, D. & Heldt, H. W. Regulation of sedoheptulose-1,7-bisphosphatase by sedoheptulose-7-phosphate and glycerate, and of fructose-1,6-bisphosphatase by glycerate in spinach chloroplasts. *Planta* **181**, 97–103 (1990).
56. Heineke, D., Bykova, N., Gardeström, P. & Bauwe, H. Metabolic response of potato plants to an antisense reduction of the P-protein of glycine decarboxylase. *Planta* **212**, 880–887 (2001).
57. Timm, S. *et al.* Glycine decarboxylase controls photosynthesis and plant growth. *FEBS Lett.* **586**, 3692–3697 (2012).
58. López-Calcagno, P. E. *et al.* Overexpressing the H-protein of the glycine cleavage system increases biomass yield in glasshouse and field-grown transgenic tobacco plants. *Plant Biotechnol. J.* **17**, 141–151 (2019).
59. Bykova, N. V., Møller, I. M., Gardeström, P. & Igamberdiev, A. U. The function of glycine decarboxylase complex is optimized to maintain high photorespiratory flux via buffering of its reaction products. *Mitochondrion* **19**, 357–364 (2014).
60. da Fonseca-Pereira, P. *et al.* Thioredoxin h2 contributes to the redox regulation of mitochondrial photorespiratory metabolism. *Plant Cell Environ.* **43**, 188–208 (2020).
61. Reinholdt, O. *et al.* Redox-regulation of photorespiration through mitochondrial thioredoxin O1. *Plant Physiol.* **181**, 442–457 (2019).
62. Eisenhut, M., Pick, T. R., Bordych, C. & Weber, A. P. M. Towards closing the remaining gaps in photorespiration - the essential but unexplored role of transport proteins. *Plant Biol.* **15**, 676–685 (2013).
63. Young, J. D. INCA: A computational platform for isotopically non-stationary metabolic flux analysis. *Bioinformatics* **30**, 1333–1335 (2014).
64. Young, J. D., Walther, J. L., Antoniewicz, M. R., Yoo, H. & Stephanopoulos, G. An elementary metabolite unit (EMU) based method of isotopically nonstationary flux analysis. *Biotechnol. Bioeng.* **99**, 686–699 (2008).
65. Antoniewicz, M. R., Kelleher, J. K. & Stephanopoulos, G. Determination of confidence intervals of metabolic fluxes estimated from stable isotope measurements. *Metab. Eng.* **8**, 324–337 (2006).
66. Farquhar, G. D., von Caemmerer, S. & Berry, J. A. A biochemical model of photosynthetic CO2 assimilation in leaves of C3 species. *Planta* **149**, 78–90 (1980).
67. Sharkey, T. D., Bernacchi, C. J., Farquhar, G. D. & Singsaas, E. L. Fitting photosynthetic carbon dioxide response curves for C3 leaves. *Plant, Cell Environ.* **30**, 1035–1040 (2007).

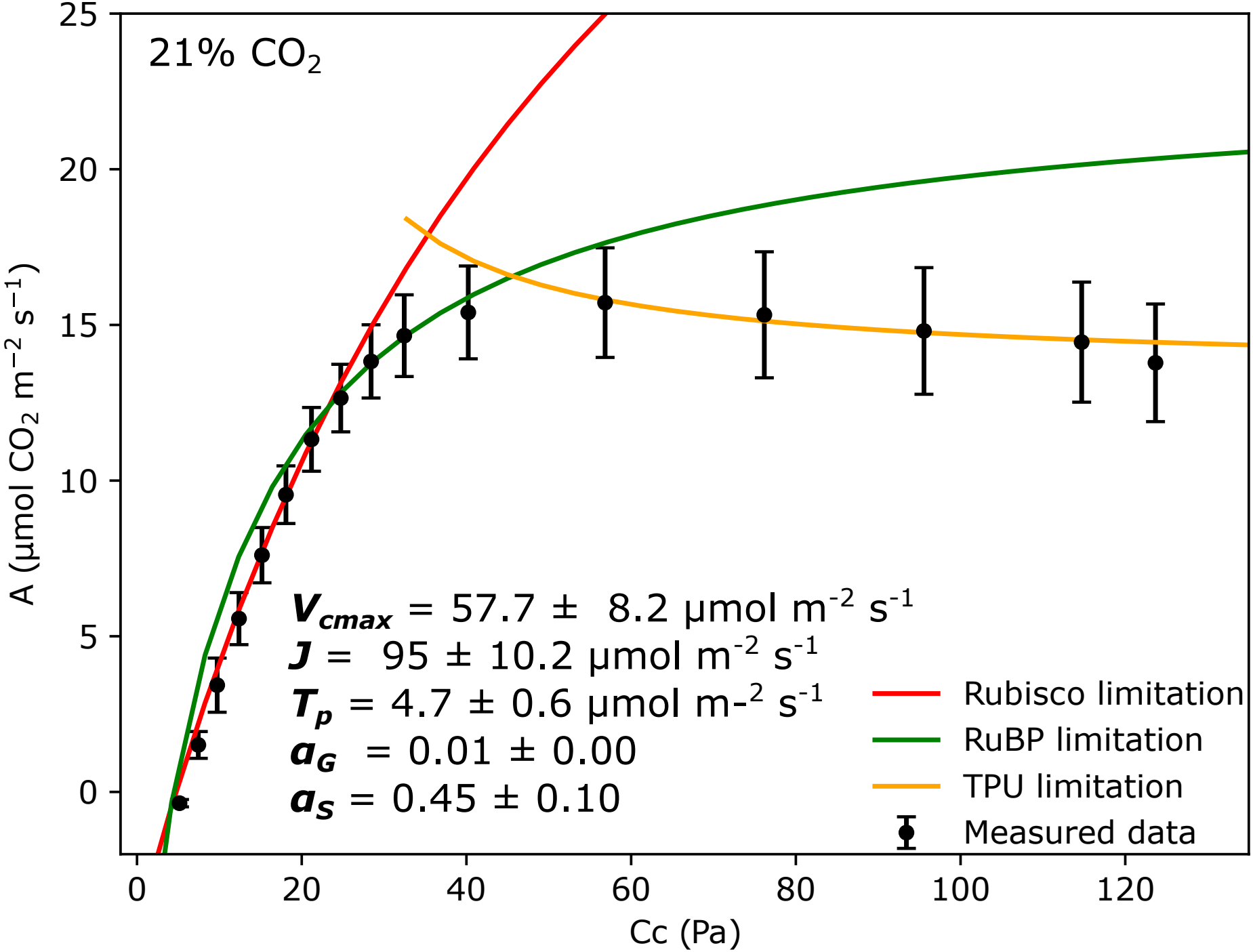
21% CO_2
V_{cmax} = 57.7 ± 8.2 µmol m^{-2} s^{-1}
J = 95 ± 10.2 µmol m^{-2} s^{-1}
T_p = 4.7 ± 0.6 µmol m^{-2} s^{-1}
a_G = 0.01 ± 0.00
a_S = 0.45 ± 0.10
Rubisco limitation
RuBP limitation
TPU limitation
Measured data
A (µmol CO_2 m^{-2} s^{-1})
Cc (Pa)
0
5
10
15
20
25
0
20
40
60
80
100
120

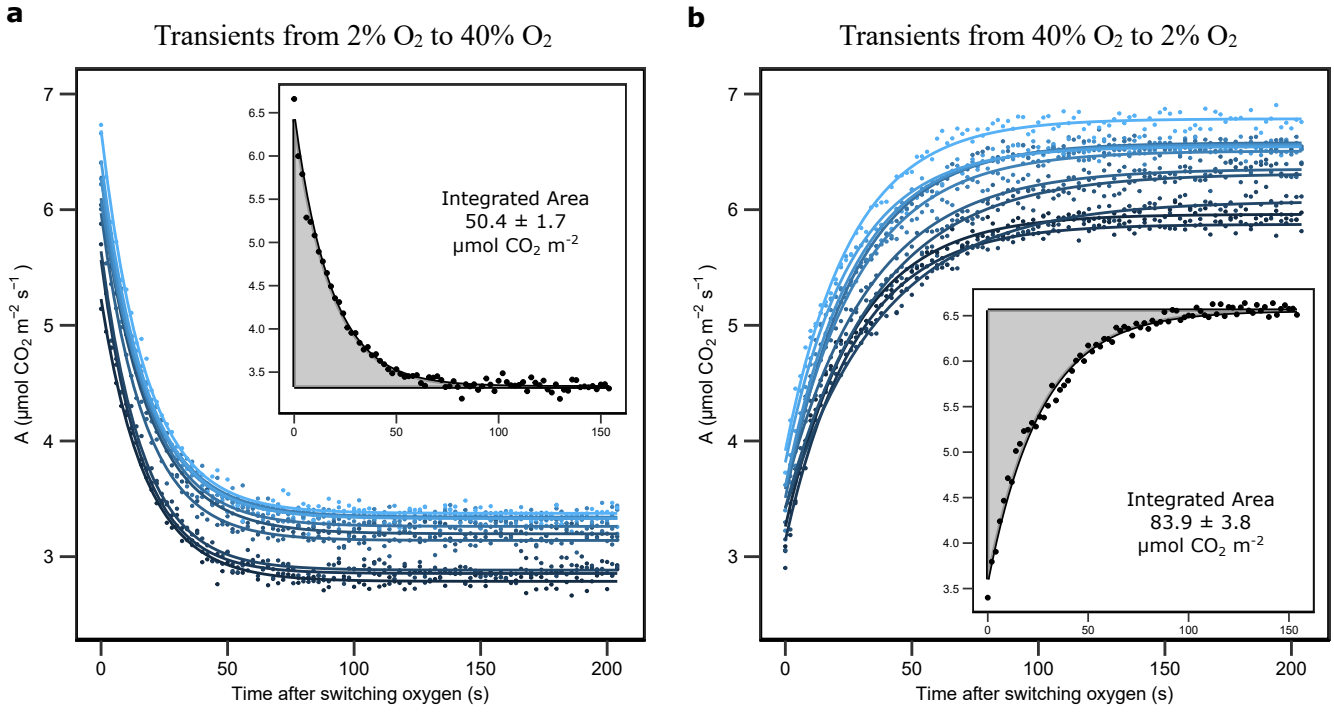
a
Transients from 2% O2 to 40% O2
A (µmol CO2 m-2 s-1)
Time after switching oxygen (s)
Integrated Area
50.4 ± 1.7
µmol CO2 m-2
b
Transients from 40% O2 to 2% O2
A (µmol CO2 m-2 s-1)
Time after switching oxygen (s)
Integrated Area
83.9 ± 3.8
µmol CO2 m-2

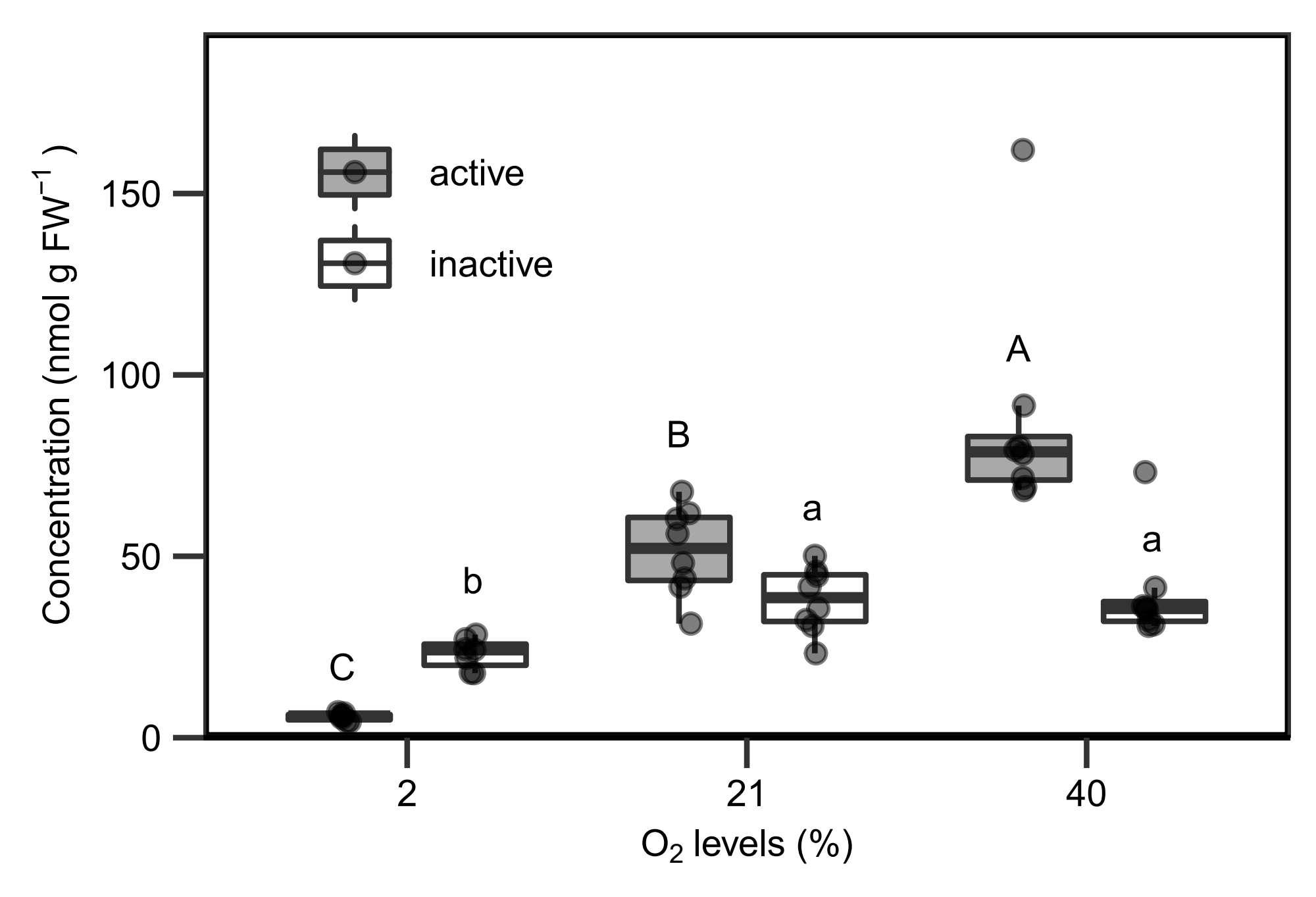
active
inactive
Concentration (nmol g FW^{-1})
150
100
50
0
C
b
B
a
A
a
2
21
40
O_2 levels (%)

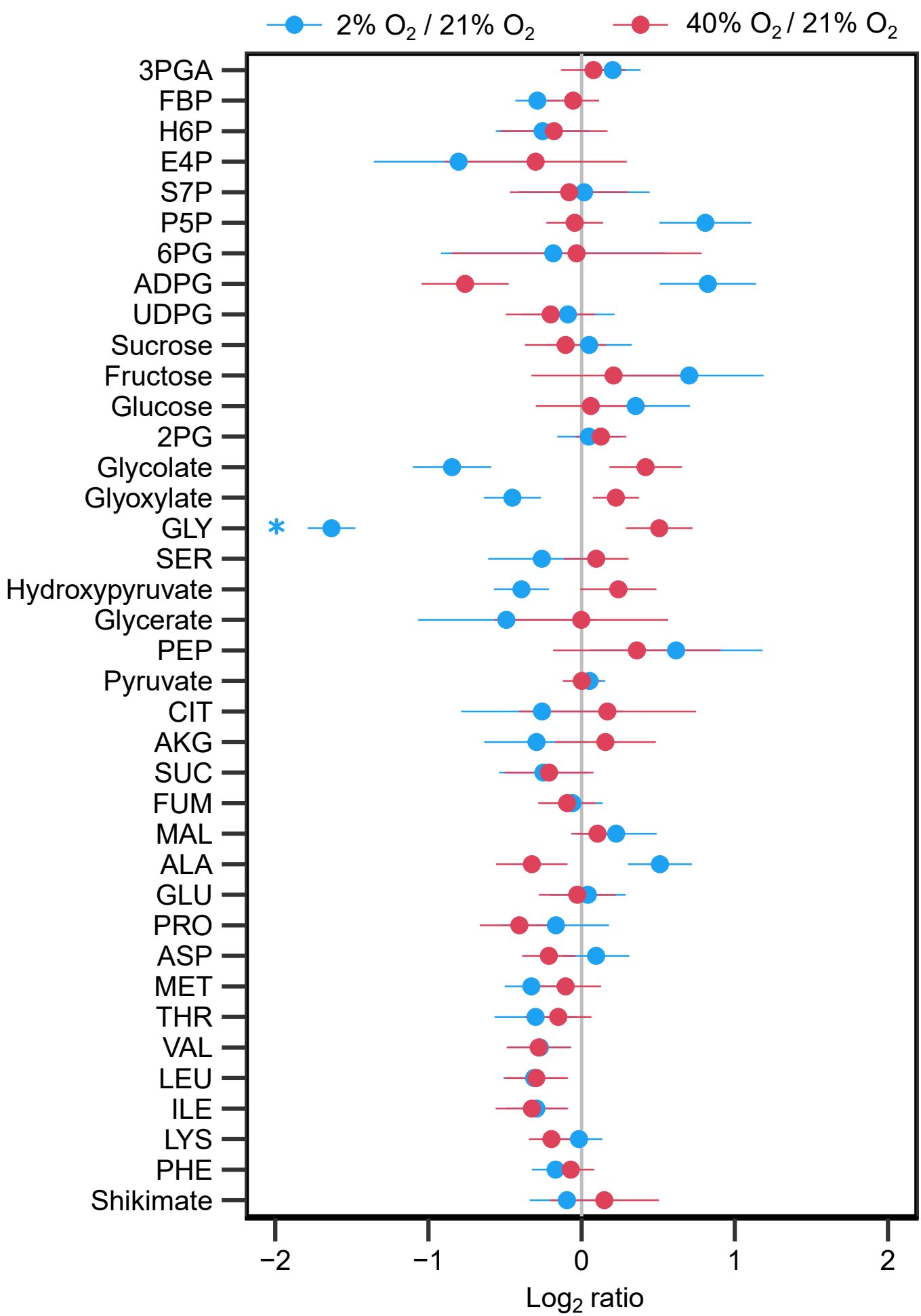
2% O2 / 21% O2
40% O2 / 21% O2
3PGA
FBP
H6P
E4P
S7P
P5P
6PG
ADPG
UDPG
Sucrose
Fructose
Glucose
2PG
Glycolate
Glyoxylate
GLY
SER
Hydroxypyruvate
Glycerate
PEP
Pyruvate
CIT
AKG
SUC
FUM
MAL
ALA
GLU
PRO
ASP
MET
THR
VAL
LEU
ILE
LYS
PHE
Shikimate
*
−2
−1
0
1
2
Log2 ratio

Supplementary Figure 1. Transient $^{13}CO_2$ labeling in selected metabolites. Experimental measurements are shown as dots with error bars (mean ± SD, n = 3 biologically independent leaves). Solid lines represent the simulated labeling kinetics obtained with our best-fit set of fluxes from INST-MFA. The nominal mass isotopologues are represented as M0 and labeled isotopologues are distinguished by their mass differences from M0 (M1, M2, M3, etc.).

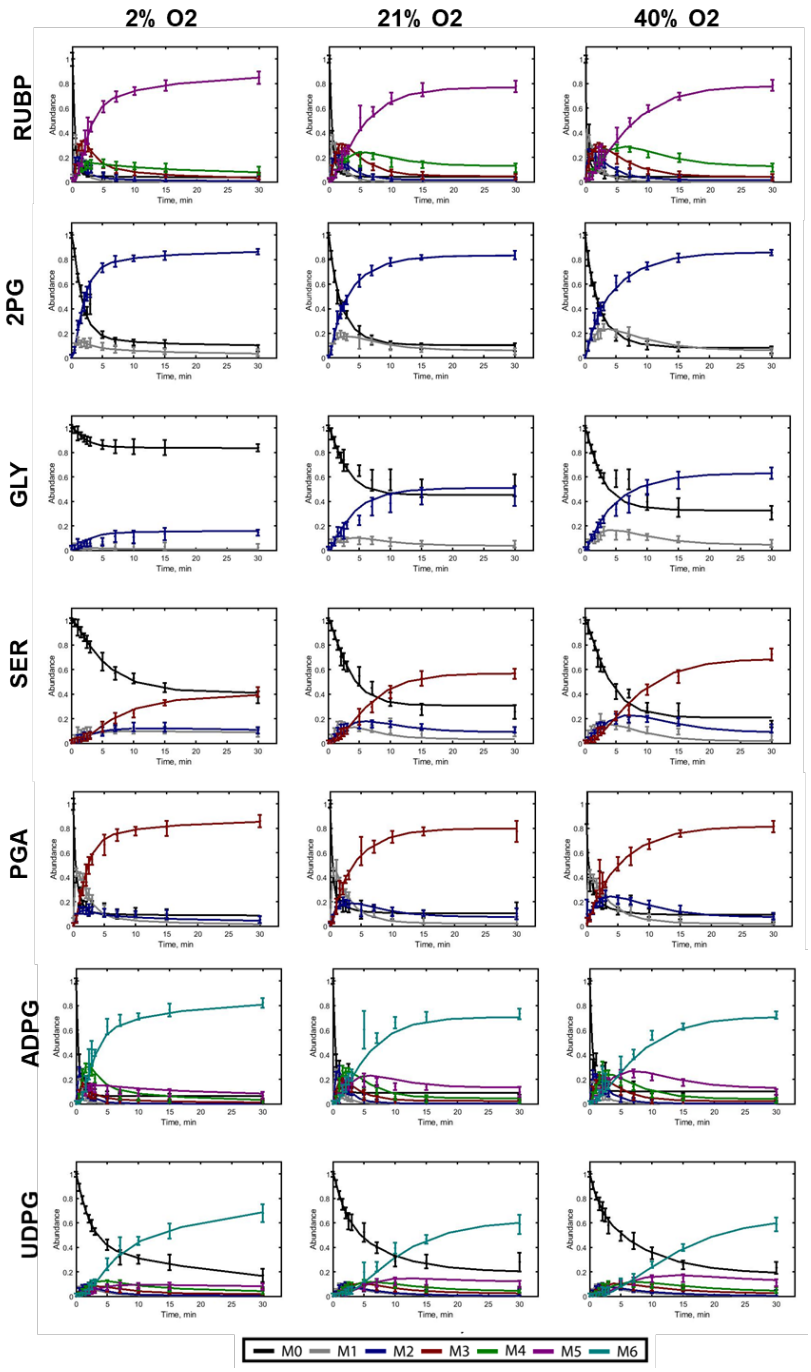

Supplementary Figure 2. Estimated fluxes and 95% confidence intervals by parameter continuation for reactions in the C3 cycle and photorespiration. Dots represent the best-fit values and horizontal lines represent the upper and lower bounds on the 95% confidence intervals calculated by the parameter continuation method. Results of all reactions are shown in a tabular form in Supplementary Data 4 and abbreviations of reactions are shown in Supplementary Data 7.

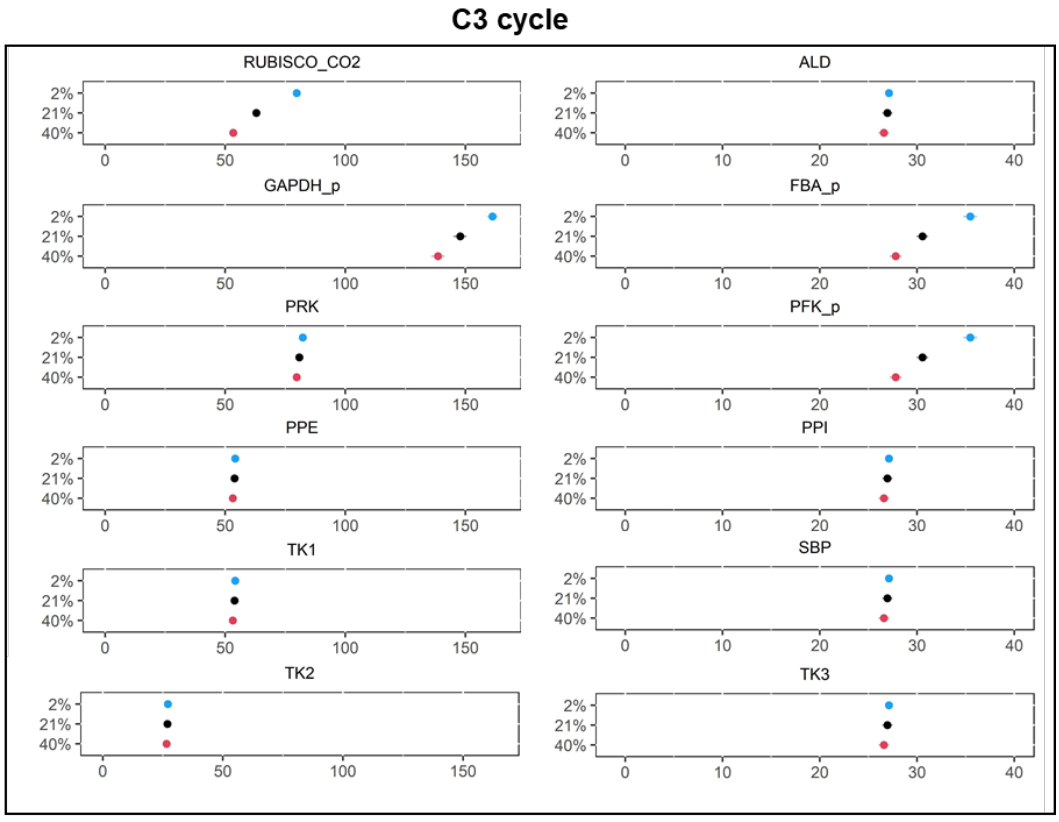

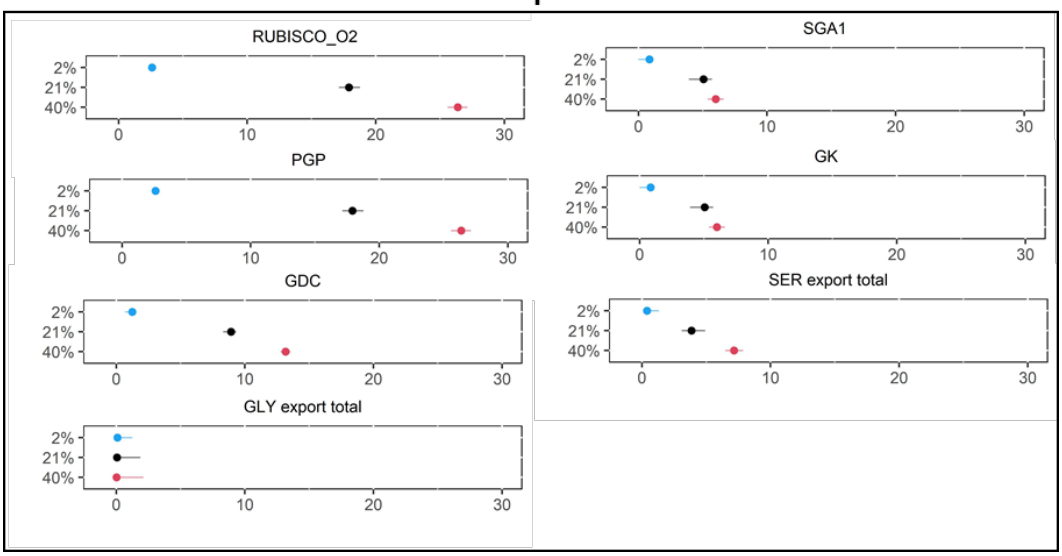

Supplementary Figure 3. Estimated flux values and 95% confidence intervals by parameter continuation for reactions in starch and sucrose synthesis and the TCA cycle. Dots represent the best-fit values and horizontal lines represent the upper and lower bounds on the 95% confidence intervals calculated by the parameter continuation method. Results of all reactions are shown in a tabular form in Supplementary Data 4 and abbreviations of reactions are shown in Supplementary Data 7.

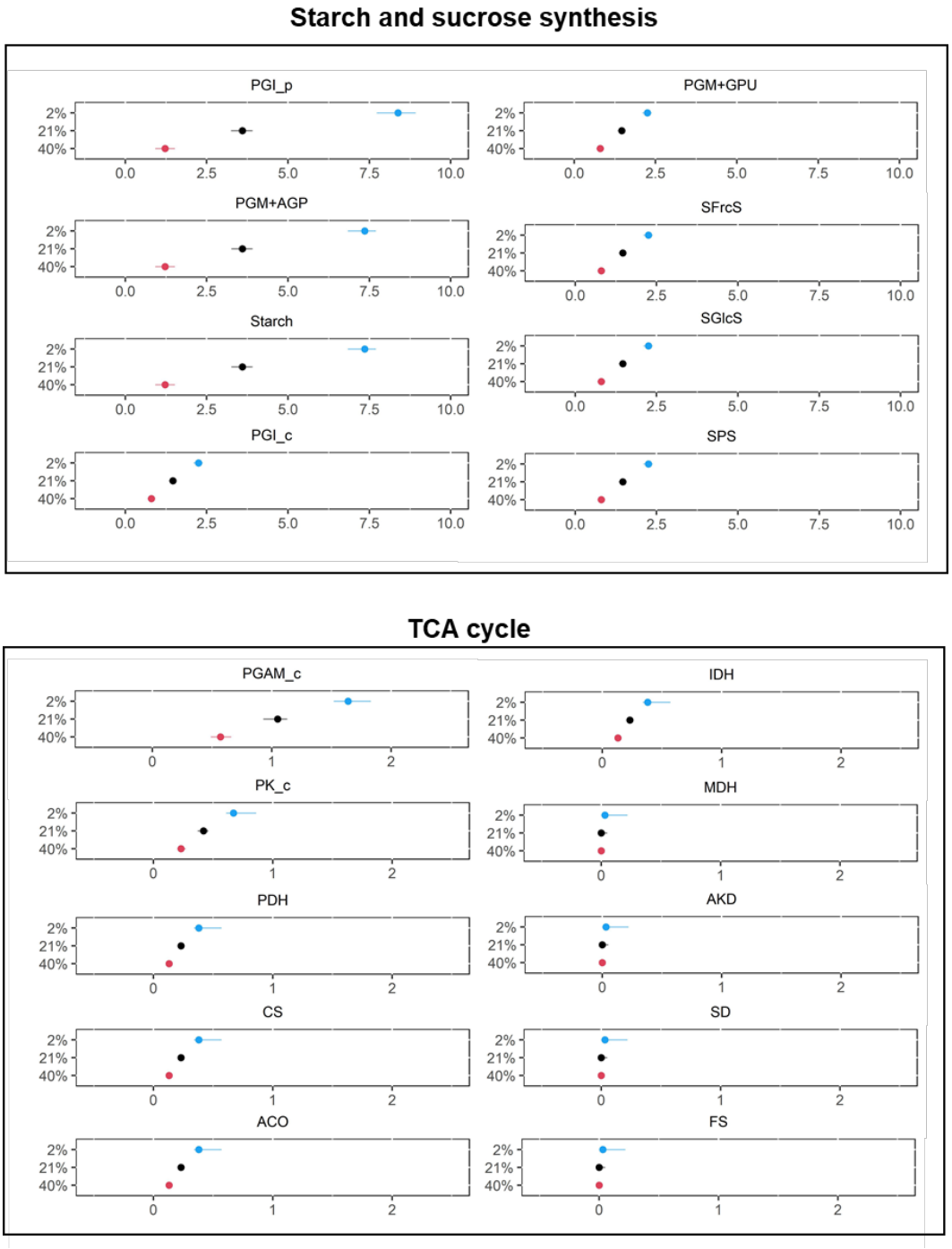

Supplementary Figure 4. The relationships between the net CO_2 assimilation rate (*A*) and synthesis rates of starch and sucrose under varied O_2 conditions. Rates of starch (A) and sucrose synthesis (B) were measured by the steady state pulse-chase labeling of $^{14}CO_2$ at each of the three O_2 conditions (see Supplementary method 2 for the estimation of starch and sucrose synthesis rates).

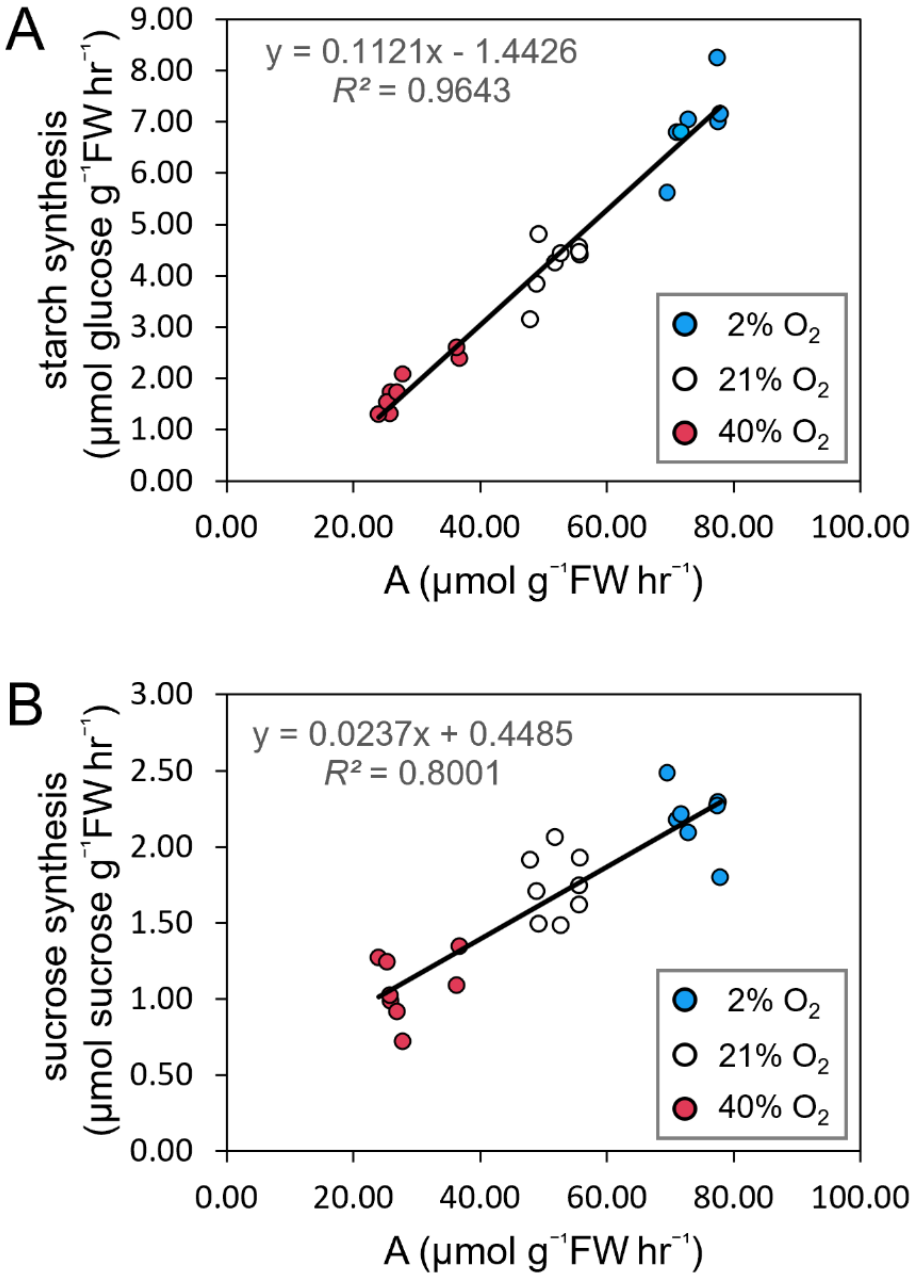

Supplementary Figure 5. Dendrogram and heatmap of the average ^{13}C-enrichment for identified metabolites over the 30 min labeling period under varying oxygen conditions. The scale of the heat map indicates blue as lowest and red as highest in the average ^{13}C-enrichment. The average ^{13}C enrichment of a metabolite was calculated by the formula of $(\frac{1}{N})\sum_{i=1}^{N} Mi \times i$, where M_i represents the fraction of the mass isotopologue distribution (MID) after natural isotope abundance correction and N represents the number of carbon atoms in the metabolite. Nominal masses of M0 mass isotopologues are shown in parentheses after metabolite names.

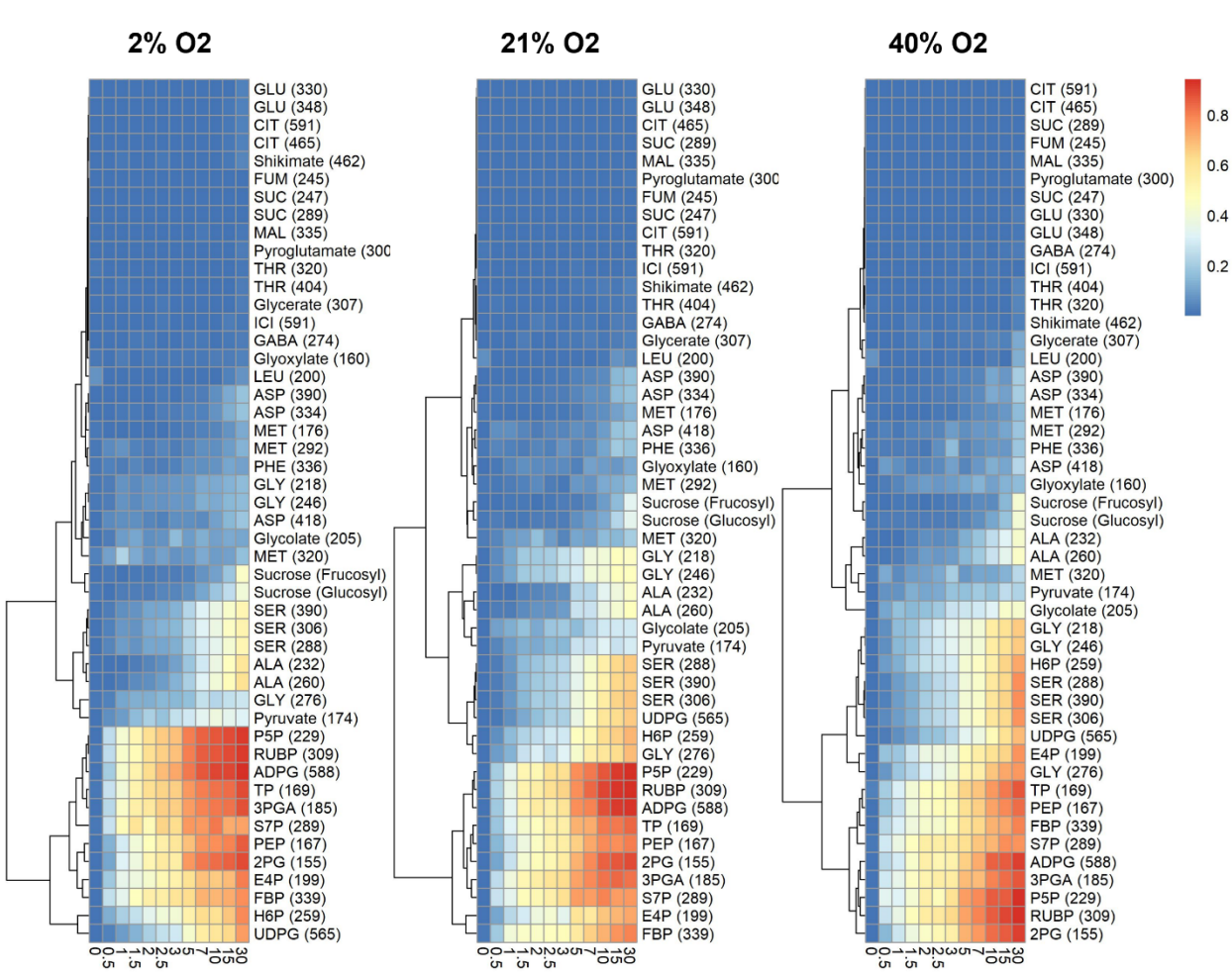

Supplementary Figure 6. Relative abundance of key metabolites (glycine, serine, and alanine) was relatively constant during the labeling period at each oxygen condition. Tobacco leaves were exposed to the three O_2 conditions in the LI-6800 cuvette for 20-30 min before incubating at 0, 0.5, 1, 2, 2.5, 3, 5, 7, 10, 15, and 30 min with $^{13}CO_2$-containing gas mixture at each oxygen condition. To assess differences in relative pool sizes of each metabolite between time-points, relative amounts of all isotopologues of a given metabolite were normalized to the internal standard and fresh weight. Data are presented as mean ± SEM (n = 3 biologically independent leaves). Total bar height represents the relative abundance of the total pool, and the shaded sections represent the fractions of isotopologues.

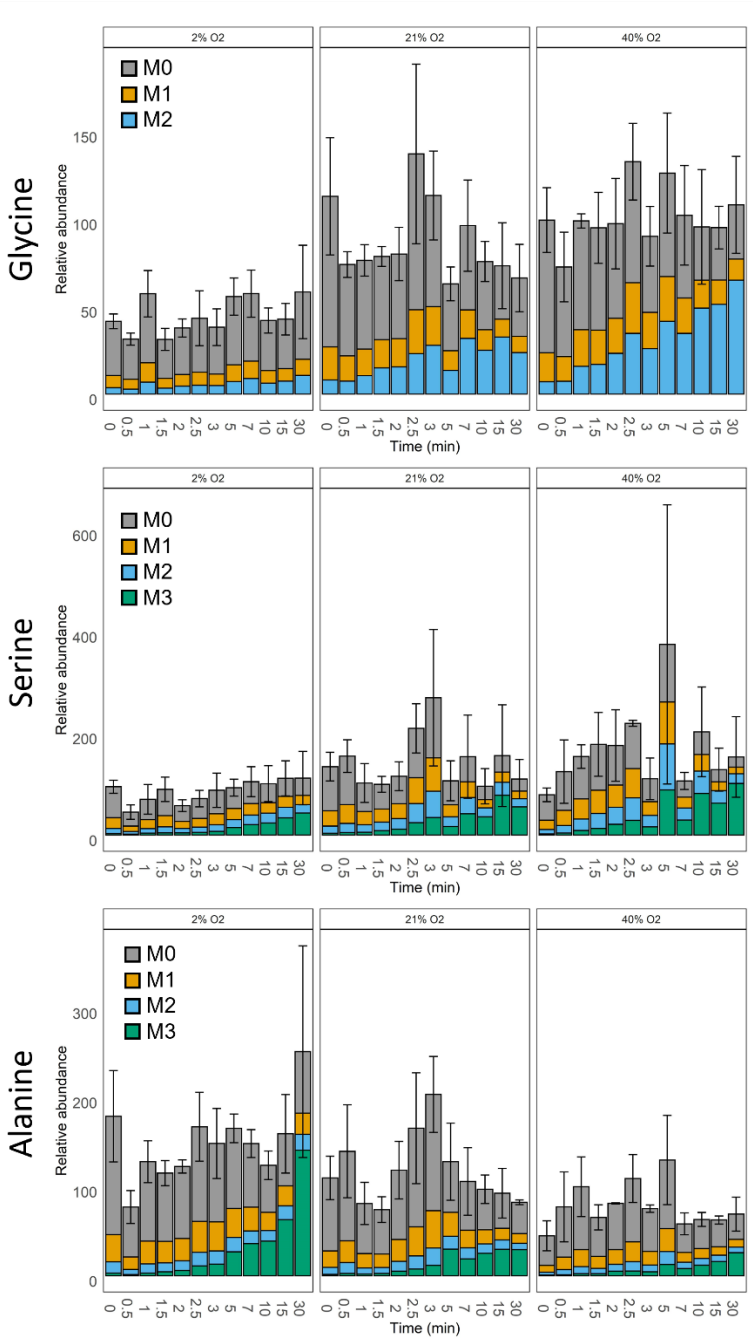

Supplementary Figure 7. Transient changes in photorespiratory intermediates (glycine, serine, and glycerate) after a switch from low to high photorespiratory condition. Leaves were acclimated under 2% oxygen for 30 min to reach the photosynthetic steady state. Samples were collected before (time = 0 s) and after (time = 60 s) switching to 40% oxygen. Data are presented as box plots (center line at the median, upper bound at 75th percentile, lower bound at 25th percentile) with whiskers extended to the extreme data point ≤ 1.5 × interquartile range from the edge of the box. Statistical significance between treatments (0 s and 60 s after switching oxygen) in each metabolite was assessed using two-tailed *t*-tests ($P < 0.05$, n = 5 biologically independent leaves). While serine and glycerate did not change during the transition, glycine increased significantly. The build-up of glycine pool after switching oxygen for 60 s was 20.6 ± 6.2 (mean ± SD) µmol m^{-2} on a leaf area basis or 65.6 ± 19.6 (mean ± SD) nmol g^{-1} FW on a fresh-weight basis.

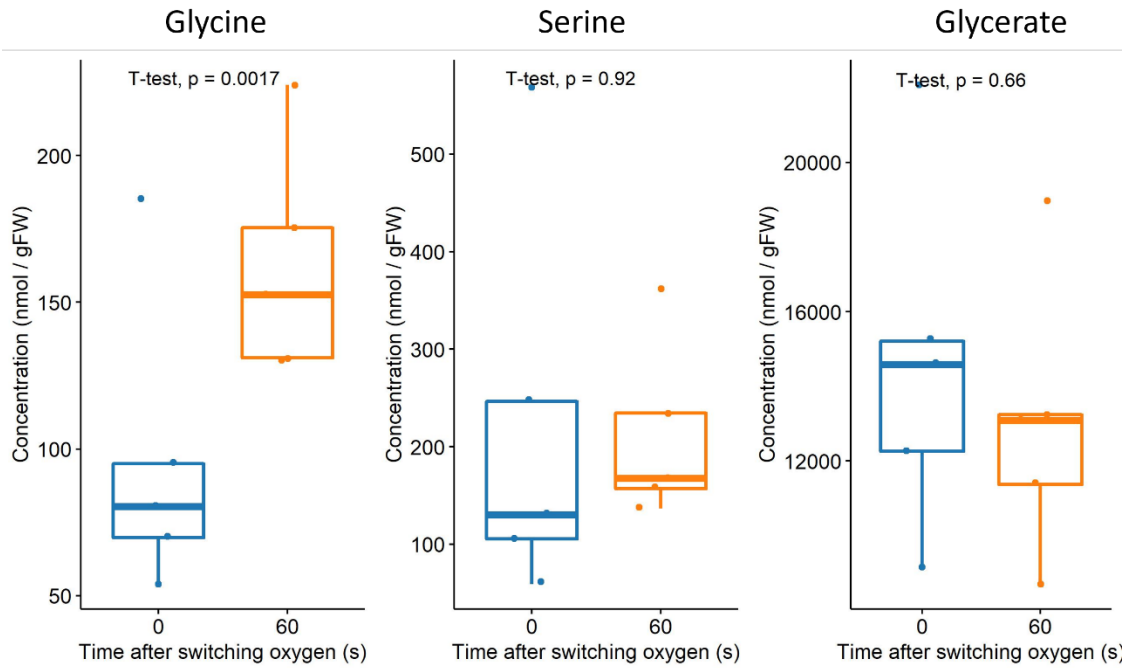

Supplementary Table 1. External flux measurements used in INST-MFA as constraints to determine intracellular fluxes. The net CO_2 assimilation rate was measured in the ^{13}C-labeled leaves using a LI-6800. Rates of rubisco carboxylation and oxygenation were calculated based on the biochemical model of photosynthesis using gas exchange data. Rates of starch and sucrose synthesis were measured by the steady state pulse-chase labeling of $^{14}CO_2$ at each of the three O_2 conditions (see Supplementary method 2 for the estimation of starch and sucrose synthesis rates). Flux values are presented as mean ± SEM (n = 7 biologically independent leaves) in units of μmol molecule g^{-1} FW hr^{-1} (for the conversion to μmol carbon g^{-1} FW hr^{-1}, multiply the presented values by the number of carbons in the molecule).

External rates	2% O_2	21% O_2	40% O_2
net CO_2 assimilation rate (μmol CO_2 g^{-1} FW hr^{-1})	74.34 ± 0.77	48.82 ± 0.76	34.11 ± 0.78
rubisco oxygenation rate[1] (μmol O_2 g^{-1} FW hr^{-1})	2.59 ± 0.06	18.8 ± 0.44	27.63 ± 0.44
rubisco carboxylation rate[1] (μmol CO_2 g^{-1} FW hr^{-1})	83.33 ± 0.77	65.92 ± 0.83	55.62 ± 0.86
starch synthesis rate (μmol glucose g^{-1} FW hr^{-1})	6.95 ± 0.29	4.22 ± 0.18	1.85 ± 0.17
sucrose synthesis rate (μmol sucrose g^{-1} FW hr^{-1})	2.19 ± 0.08	1.72 ± 0.07	1.09 ± 0.07

[1] The calculation of rubisco carboxylation and oxygenation rates requires the determination of three gas exchange parameters. The mesophyll conductance (g_m), respiration in the light (R_L) and the CO_2 compensation point in the absence of mitochondrial respiration (Γ^*) were determined to be 2.00 μmol m^{-2} s^{-1} Pa^{-1}, 0.67 μmol m^{-2} s^{-1}, and 4.04 Pa (see Supplementary Method 4 for details of calculations).

Supplementary Table 2. Sucrose and amino acid levels in vascular exudates. Vascular exudates were collected using a pressure bomb chamber to force release of liquid from the petiole of a fresh cut tobacco leaf previously exposed to ambient oxygen (21%) and analyzed by GC-MS (see Supplementary Method 1). Values of the levels are mean ± SEM (n = 9 biologically independent leaves). The ratios of several amino acids to sucrose (Glutamate (GLU) / Sucrose = 0.159, Aspartate (ASP) / Sucrose = 0.270, Alanine (ALA) / Sucrose = 0.128, Glycine (GLY) / Sucrose = 0.042, Serine (SER) / Sucrose = 0.168) were used to constrain the output flux reaction (S6P + 0.159*GLU + 0.27*ASP + 0.129*ALA.c + 0.042*dummyGLY + 0.169*dummySER -> Sink) in all INST-MFA models. The amino acid to sucrose ratios were comparable to those measured in the aphid stylet-collected phloem sap[1].

Metabolite	**Level (nmol/μL)**
Sucrose	0.403 ± 0.063
ASP	0.1 ± 0.021
SER	0.069 ± 0.017
GLU	0.064 ± 0.013
ALA	0.048 ± 0.008
GLY	0.014 ± 0.001

[1] Winter, H., Lohaus, G. & Heldt, H. W. Phloem transport of amino acids in relation to their cytosolic levels in barley leaves. Plant Physiol. 99, 996–1004 (1992).

Supplementary Method 1. The extraction and analytical procedures for quantifying metabolite labeling and concentration.

1.1 Harvesting and quenching

For the $^{13}CO_2$ labeling experiment at each O_2/N_2 condition (2% O_2 / 98% N_2, 21% O_2/ 79% N_2, or 40% O_2/ 60 % N_2), labeled tobacco leaf samples were collected at time points of 0, 0.5, 1, 2, 2.5, 3, 5, 7, 10, 15, 30 min inside the 9 cm^2 cuvette of a LI-COR 6800 (LI-COR Biosciences, USA) with at least three biological replicates. To quench metabolism rapidly under illumination at a given time point, liquid nitrogen was directly sprayed on the leaf surface by inserting a liquid nitrogen cryospray nozzle (Wallach UltraFreeze, Cooper Surgical, USA) via an injection port on the LI-COR cuvette. The frozen leaf potions were rapidly removed from the cuvette, then cut and placed in a tube with liquid nitrogen and stored at -80°C until analysis before they were thawed. This sampling procedure has been extensively described earlier [1] with pictures of the setup and measurements of the $^{13}CO_2$ switching and quenching speed.

To determine the steady-state pool sizes of central metabolites in leaves exposed to the three O_2/N_2 conditions (all at 40 Pa $^{12}CO_2$ levels), leaves were put in the LI-COR cuvette for 30 min to acclimate until they reached a photosynthetic steady-state. At least seven biological replicates for each condition were harvested and quenched as described earlier.

To measure the vascular sucrose and amino acids, exudates were collected using a pressure bomb chamber on plants harvested under ambient conditions. A fresh cut tobacco leaf was placed inside the chamber, with the cut end of the petiole protruding from the rubber seal of the chamber. Pressure was gradually applied from a gas cylinder until droplets of liquid appeared at the cut surface. Exudates were collected from nine randomly chosen mature leaves in different plants. The exudate collection was carried out in the same condition for each replicate within 3 min to avoid dehydration and lack of light. Samples were subsequently frozen in liquid nitrogen and stored at −80°C for further analysis.

To determine the transient changes in metabolite pool sizes after a switch from low to high photorespiratory condition, leaves were first put in the LI-COR cuvette under low oxygen (40 Pa $^{12}CO_2$, 2% O_2, and 98% N_2) for 30 min. After the leaves reached the photosynthetic steady-state, five low-oxygen adapted leaves were quenched and collected immediately. The other five leaves were quenched and collected after the gas in the cuvette was switched to high oxygen (40 Pa $^{12}CO_2$, 40% O_2, and 98% N_2) for 1 min. In all experiments, leaves were randomly assigned to one of the treatments or time points.

1.2 Metabolite extraction of polar metabolites

Frozen leaf tissues were pulverized under cryogenic conditions using a FastPrep-24 tissue homogenizer with a CoolPrep Adapter (MP biomedicals, USA). Metabolites were extracted using a methanol/chloroform/water protocol as described earlier [2]. The extracts were separated into upper (methanol/water) phase and bottom (chloroform) phase after centrifugation. Several aliquots of polar extracts were taken from the upper layer, lyophilized to dryness, and frozen at -80°C before the GC-MS and LC-MS/MS analyses. For pool size quantification of unlabeled samples, known concentrations of internal standards (nor-Leucine, 98 atom % ^{15}N, 98 atom % ^{13}C free amino acid mixture, D-[UL-$^{13}C_6$] fructose 1, 6-bisphosphate, and [UL-$^{13}C_{12}$] sucrose) were spiked onto the tissue before the extraction.

1.3 Gas chromatography- mass Spectrometry (GC-MS) analyses

Organic acids, amino acids, and sugars recovered in the polar fractions were first derivatized by adding methoxyamine hydrochloride dissolved in dry pyridine. The reaction mixture was shaken at 90 rpm at 40°C for 12 h. An aliquot of the reaction mixture was silylated by adding N, O-Bis (trimethylsilyl)

trifluoroacetamide with 1% (w/v) trimethylchlorosilane and incubated at 60°C for 60 min, resulting in trimethylsilyl (TMS) derivatives. Another aliquot of the reaction mixture was silylated by adding N-(tert-butyldimethylsilyl)-N-methyltrifluoroacetamide with 1% (w/v) tert-butyldimethylchlorosilane and incubated at 60°C for 60 min, resulting in trimethylsilyl (TBDMS) derivatives. The TMS- and TBDMS-derivatives were analyzed by an Agilent 7890A GC (Agilent, USA) equipped with a 30 m VF-5ms column and interfaced to an Agilent 5975C inert XL Mass Selective Detector (Agilent, Santa Clara, CA, USA). Aliquots of the derivatized sample (1 µL) were injected in splitless mode with a helium carrier gas flow set at 1 mL/min. For some highly abundant metabolites (e.g., malate, fumarate, glycerate, and sucrose, etc.), a split mode with a 20:1 split ratio was applied. The inlet temperature and MS transfer line temperature were set at 230°C and 300°C, respectively. The oven temperature was initially held at 40°C for 1 min, then raised at 40°C/min to 80°C, ramped at 10°C/min to 240°C, then 20°C/min to 320°C, and finally kept at this temperature for 5 min. The mass spectrometer was operated on scan mode (electron impact at 70 eV, ion source temperature at 230°C, the quadrupole temperature at 150°C), monitoring ions at m/z values of 50–600.

GC-MS data files were deconvoluted and searched against the NIST 14 Mass Spectral Library and the Golm Metabolome Database using NIST software AMDIS V2.72 for initial identification. Chromatographic peaks were further identified based on the retention time of authentic standard peaks and the corresponding MS spectrum. The characteristic fragment ions that were used for the isotopologue analysis are shown in Supplementary Data 6. The mass isotopologue distribution (MID) for each metabolite was correct for natural abundance of isotopes and mean ^{13}C enrichment was calculated as described earlier [3]. The EI spectrum of the TMS derivative of sucrose cannot be directly used for the isotopologue analysis, as each of the two major fragment ions m/z 361 and 451 represents a mixture of glucosyl and fructosyl moieties of sucrose. The fragmentation patterns of [UL-$^{13}C_6$fru] sucrose was used to deduce the proportion of the glucosyl and fructosyl moieties in each fragment ion. Fragment m/z 361 corresponds to a mixture of 54% fructosyl and 46% glucosyl unit. Fragment m/z 451 is a mixture of 96% fructosyl and 4% glucosyl. The actual MIDs of glucosyl and fructosyl moieties of sucrose were solved using the m/z 361-367 and 451-457 as described earlier[3].

1.4 Ion-pair chromatography – tandem mass spectrometry (IPC-MS/MS) analyses

Phosphorylated intermediates in C3 cycle were analyzed by an IPC-MS/MS method as described earlier[1]. Aliquots of freshly reconstituted lyophilized extract (10 µL) were injected into a Waters ACQUITY UPLC pump system (Waters, USA) coupled to a Waters Quattro Premier tandem quadrupole mass spectrometer in negative-mode electrospray ionization (ESI). Chromatographic separation was performed using a Waters UPLC BEH C18 column (2.1× 50 mm) at 40°C using a multi-step gradient with eluent A (10 mM tributylamine in 5%(v/v) methanol, adjusted to pH 6 with 0.5 M acetic acid) and eluent B (methanol): 0-1 min, 95-85% A; 1-6 min, 65-40% A; 6-7 min, 40-0% A; 7-8 min, 0% A; 8-9 min, 100% A. The flow rate was 0.3 mL min^{-1}, source temperature 120°C, and desolvation temperature 350°C. The parent-product ion pairs for each metabolite and the specific metabolite-dependent MS parameters are shown in Supplementary Data 6.

1.5 Anion exchange chromatography – tandem mass spectrometry (AEC-MS/MS) analyses

Nucleotide sugars (ADPG and UDPG) and additional phosphorylated intermediates (i.e., 2PG, PEP) were analyzed by AEC-MS/MS as described earlier [1]. Aliquots of freshly reconstituted lyophilized extract (10 µL) were analyzed by a Waters ACQUITY UPLC pump system coupled to a Xevo ACQUITY TQ Triple Quadrupole Detector (Waters, USA) in negative-ESI mode. Chromatographic separation was performed using an IonPac AS11 analytical column (Dionex, 2 × 250 mm) coupled to an IonPac guard column AG11

(2 × 50 mm, Dionex, Thermo Scientific, USA) and an IonPac ATC-3 Anion Trap Column (4 × 35 mm, Dionex, Thermo Scientific, USA) using a multi-step gradient with eluent A (0.5 mM KOH) and eluent B (75 mM KOH): 0-2 min, 100% A; 2-4 min, 100-93% A; 4-13 min, 93-60% A; 13-15 min, 0% A; 15-17 min, 100% A, at a flow rate of 0.35 mL min^{-1}. Salt suppression was carried out using a post-column anion self-regenerating suppressor (Dionex ADRS 600, Thermo Scientific, USA), operated in the AutoSuppression External Water mode with a flow rate of 3.5 mL min^{-1} and current of 50 mA. The parent-product ion pairs for each metabolite and the specific metabolite-dependent MS parameters are shown in Supplementary Data 6.

1.6 Data analysis for metabolite labeling and profiling data

Chromatographic peaks for LC-MS/MS and GC-MS were integrated using the Waters software MassLynx version 4.2 and DExSI version 1.11 (https://github.com/DExSI/DExSI/). For natural isotope abundance correction, the measured mass isotopologue distributions determined from the GC-MS and LC-MS/MS data were subsequently processed using Fluxfix version 0.1 (https://fluxfix.science/). Statistical analysis of metabolite labeling and profiling data was performed in R version 4.0.2.

Supplementary Method 2. Steady state pulse-chase labeling of $^{14}CO_2$ to estimate rates of starch and sucrose accumulation at varying O_2 conditions

Fully expanded tobacco leaves were pulsed with $^{14}CO_2$ at each of the three O_2/N_2 conditions (2% O_2 / 98%N_2, 21% O_2/ 79% N_2, and 40% O_2/ 60 % N_2) through the sample port on the back of a head of a LI-6800 (LI-COR Biosciences, USA) for 10 min. The assimilated ^{14}C was then chased with $^{12}CO_2$ for 5 min, under a light intensity of 100 µmol photon m^{-2} s^{-1} and temperature of 25°C. The leaves were exposed to CO_2 concentrations of 400 µL L^{-1} (v/v) during the entire pulse-chase labeling process. At the end of the chase period, the labeled leaf tissue was immediately frozen in liquid nitrogen and stored at −80°C. Frozen tissue was extracted with 0.5 mL formic acid solution (formic acid/ethanol 4:75, v/v). The suspension was centrifuged at 12000 g, 4˚C for 10 min. Half of the supernatant was directly counted for radioactivity (total soluble fraction) using a 1450 Microbeta Trilux scintillation counter (Perkin Elmer, USA). The other half the supernatant was passed through a Dowex 1 (Cl^- form) column, followed by a Dowex 50 (H^+ form) column. The first 1 mL flow through was discarded and the next five 1 mL fractions were separately collected and counted for radioactivity (neutral soluble fraction). The ionic fraction was calculated as the difference in radioactivity between total soluble fraction and the neutral soluble fraction. The pellet was washed once with water and twice with 80 % ethanol and then resuspended in 0.5 mL of 0.2 M KOH. Starch in the pellet was gelatinized at 95 °C for 30 min, then digested with 50 U alpha -amylase and 6.5 U amyloglucosidase in an acetate buffer (pH 5) for 2 days. After centrifugation, the supernatant was removed and counted for radioactivity. Proportion of counts in the starch and neutral soluble fraction (presumably mostly sucrose) relative to total counts were multiplied by the photosynthetic rate of each leaf to estimate rates of starch and sucrose accumulation. Due to the relatively large sucrose pool and slow turnover rate, we assume that the loss of sucrose exported from the labeled leaf region during the short labeling period is negligible.

Supplementary Method 3. Determining diffusional and biochemical parameters for estimating rates of rubisco oxygenation (v_o) and rubisco carboxylation (v_c).

3.1 Describing the Gas-Exchange and Carbon Isotope Discrimination System

To estimate $g_{m,}$ which is required to calculate the intercellular CO_2 concentrations needed to estimate v_o and v_c, *in vivo* gas exchange measurements of steady-state photosynthesis were combined with on-line measurements of carbon isotope discrimination, Δ , as described earlier[4-6] using a LI-6800 (LI-COR

Biosciences, USA) coupled to a tunable infrared laser differential absorption spectrometer (TILDAS-CS, Aerodyne Research, USA).

A computer-controlled front-end was provided for the system, as an integrated hardware and software system "Vinland" created by H. Stuart-Williams at the Australian National University (Contact information available upon request). In brief, software running on a PC/Arduino pair reads and displays output from the laser and controls hardware devices including valves (VICI Valco Instruments Co. Inc., USA) and mass flow controllers (Alicat Scientific, Inc., USA) to manage a gas mixing system to make synthetic air and dope it with isotopically characterized reference CO_2 as required, using pneumatic injection valves with capillaries (SGE MOVPT, SGE International, Ringwood, Australia).

The fully expanded leaf was placed across the leaf chamber avoiding the midrib. The CO_2 in the leaf chamber, flow rate, and irradiance were set to 400 μmol mol^{-1}, 300 μmol s^{-1}, 1750 μmol m^{-2} s^{-1}, respectively. The LI-6800 was located inside a heating cabinet (Percival Scientific, USA) to maintain a 25°C leaf temperature and a 1.2 kPa vapor pressure deficit throughout the measurement. One synthetic air line was bubbled through a flask of water and fed into the LI-6800 air inlet port. A separate isotope reference line was doped with a specified concentration of CO_2 ($\delta^{13}C$ vs. VPDB: -4.6 ‰, (Airgas Specialty Gases, USA)) to produce a calibration reference line to correct the raw $\delta^{13}C$ signals. To determine Δ, the reference and sample exhaust lines of the LI-6800 were subsampled into the TILDAS-CS on an alternating basis. To accomplish this, two lines connected the LI-6800 exhaust ports A and B carried sample and reference airstreams through Nafion tubing and a dry-ice ethanol trap to remove all water vapor from the airstream. These lines and the calibration reference line from the mixing system, were connected to separate ports on the VICI multiposition valve to switch airstreams entering the TILDAS-CS. The TILDAS-CS measured molar ratios of the different carbon dioxide isotopologues ($^{16}O^{12}C^{16}O$, $^{16}O^{12}C^{17}O$, $^{16}O^{12}C^{18}O$ & $^{16}O^{13}C^{16}O$). Scripts running in the Vinland software controlled the valves and mixing and calculated/averaged raw $\delta^{13}C$ values for each measurement period.

$\delta^{13}C$ was calculated as:

$$\delta^{13}C = \left(\frac{R_{sample}}{R_{standard}} - 1\right) * 1000 \quad (1)$$

where R_{sample} is the molar ratio of the fractional abundance of the heavy isotope over the fractional abundance of the light isotope from the airstream that is measured by the TILDAS-CS, $\frac{^{16}O^{13}C^{16}O}{^{16}O^{12}C^{16}O + {}^{16}O^{12}C^{17}O + {}^{16}O^{12}C^{18}O}$. While the $R_{standard}$ is the molar ratio of Vienna Pee Dee Belemnite, the international reference standard for $^{13}C/^{12}C$ and is 0.0111797 [4].

The TILDAS-CS was calibrated using an offset calibration approach as described earlier [4] to correct the raw $\delta^{13}C$. With the corrected $\delta^{13}C$, the observed ^{13}C photosynthetic discrimination, Δ_{obs}, was calculated from an equation presented in [4,7]:

$$\Delta_{obs} = \frac{\zeta\left(\delta^{13}C_{sample} - \delta^{13}C_{reference}\right)}{1 + \delta^{13}C_{sample} - \zeta\left(\delta^{13}C_{sample} - \delta^{13}C_{reference}\right)} \quad (2)$$

$$\zeta = \frac{^{12}CO_{2;\,reference}}{^{12}CO_{2;\,reference} - {}^{12}CO_{2;\,sample}} \quad (3)$$

where $\delta^{13}C_{sample}$ and $\delta^{13}C_{reference}$ are the carbon isotope compositions of the sample and reference airstreams coming from the LI-6800. ζ is the ratio of the $^{12}CO_2$ mole fraction in the dry air coming into the gas-exchange cuvette over the difference in $^{12}CO_2$ mole fractions of air in and out of the cuvette [4].

3.2 Measurement Cycle

To find accurate Δ_{obs} values, the system needed to cycle the calibration reference line and the LI-6800 sample and reference lines to determine the $\delta^{13}C$ of the gases. A Vinland script automated the calibration and sampling analysis. The calibration reference line was measured at two different concentrations (39 and 46.5 Pa) at the beginning and end of the measurement cycle. In-between the calibration measurements were the LI-6800 reference and sample measurements. These lines were subsampled five times to produce five technical replicates within one measurement cycle. An autolog program was written on the LI-6800 GUI to match the timing of the Vinland script so that gas-exchange measurements could be taken simultaneously with the carbon isotope discrimination measurements.

Measurements were corrected using an offset calibration. Offsets were calculated from the true (-4.6 ‰) and measured calibration reference $\delta^{13}C$ values at each CO_2 concentration. With these offsets, a linear regression was modeled between the CO_2 concentrations and offsets to create an offset calibration line. This offset calibration line was applied to correct the raw $\delta^{13}C$ measurements [4].

3.3 Final Estimation of g_m

Estimation of g_m was performed using the online isotope data according to [4,5]

$$g_m = \frac{1+t}{1-t}\,\frac{b'_3 - a_m - \frac{\alpha_b}{\alpha_e}e\frac{R_L}{A-R_L}}{\frac{\bar{a}}{1-t}+\frac{1}{1-t}[(1+t)*b'_3-\bar{a}]\frac{C_i}{C_a}-\frac{1+t}{1-t}\frac{\alpha_b}{\alpha_e}e\frac{R_L}{A-R_L}\frac{C_i-\Gamma^*}{C_a}-\frac{1+t}{1-t}\frac{\alpha_b}{\alpha_f}f\frac{\Gamma^*}{C_a}-\Delta_{obs}}\,\frac{A}{C_a} \quad (4)$$

where, $t = \frac{\alpha_{ac}E}{2g_{ac}}$, and $\bar{a} = \frac{a_b(C_a-C_s)+a_s(C_s-C_i)}{C_a-C_i}$. e was calculated with the assumption that the plant used old photosynthate as the substrate for respiration, $e = \delta^{13}C_{tank} - \delta^{13}C_{atmosphere}$, where $\delta^{13}C_{tank}$ was the measured $\delta^{13}C$ of the sample airstream, and the $\delta^{13}C_{atmosphere}$ was assumed to be -8‰. R_L and Γ^* values were used from the common intersection method (described below). Other variables and fractionation factors used in the equation 4 are defined in the table below as described earlier [4].

Variable (units)	Definition
A (μmol m^{-2} s^{-1})	Net CO_2 assimilation rate
a_b (‰)	$^{12}C/^{13}C$ fractionation for CO_2 diffusion in the boundary layer (a_b = 2.9‰)
a_m (‰)	Summed $^{12}C/^{13}C$ fractionation during the liquid-phase dissolution and dissolution of CO_2 diffusion in the boundary layer (a_m = 1.8 ‰)
a_s (‰)	$^{12}C/^{13}C$ fractionation for CO_2 diffusion in air (a_s = 4.4‰)
$\bar{a}$ (‰)	The weighted fractionation for CO_2 diffusion across boundary layer and stomata in series
b'_3 (‰)	Overall *in vivo* $^{12}C/^{13}C$ fractionation during carboxylation by rubisco and PEPC (b'_3 = 30‰)

C_a (Pa)	The CO_2 partial pressure in the ambient air
C_i (Pa)	The CO_2 partial pressure in the intercellular airspace of the leaf
C_i^* (Pa)	The CO_2 partial pressure in the intercellular airspace of the leaf at the photorespiratory CO_2 compensation point
C_s (Pa)	The CO_2 partial pressure at the leaf surface
E (mol m^{-2} s^{-1})	Transpiration rate
e (‰)	$^{12}C/^{13}C$ fractionation during decarboxylation
f (‰)	$^{12}C/^{13}C$ fractionation during photorespiration (f = 11.8‰)
g_{ac} (mol m^{-2} s^{-1})	Conductance to diffusion of CO_2 in air
R_L (μmol m^{-2} s^{-1})	Non-photorespiratory CO_2 release in the light
t	Ternary correction coefficient
α_{ac}	$\alpha_{ac} = 1 + \bar{a}$
α_b	$\alpha_b = 1 + b'_3$
α_e	$\alpha_e = 1 + e$
α_f	$\alpha_f = 1 + f$
Γ^* (Pa)	The CO_2 partial pressure in the chloroplast at the photorespiratory CO_2 compensation point

3.4 Measurement of C_i^* and R_L

To measure C_i^* and R_L, we used the common intersection method [8,9]. As described above, measurements were performed using a LI-6800. The LI-6800 maintain a 25°C leaf temperature, a 1.5 kPa vapor pressure deficit, and a flow rate of 500 μmol s^{-1} during the measurement. The common intersection method measurements were linear fits of CO_2 response curves measured at 3, 5, 7, 9, 11, 40 (Pa) at irradiances of 250, 165, 120, 80, 50 (μmol m^{-2} s^{-1}). C_i^* and R_L values were determined from the linear regression of the slopes and y-intercepts from each irradiance as described earlier [9,10].

3.5 Calculating Γ^*

Γ^* was determined from $\Gamma^* = C_i^* + \frac{R_L}{g_m}$, where g_m, C_i^*, and R_L were determined from the gas exchange, and carbon isotope discrimination approaches described earlier [11]. g_m and Γ^* were resolved iteratively using previous g_m, Γ^*, and R_L values to improve solutions accuracy; iterations were stopped when unity was reached. Gas exchange and stable carbon isotope data were analyzed using R; scripts will be available upon request.

3.6 Calculating v_o and v_c

The key equation for estimating v_o and v_c using measured rates of A is

$$A = v_c - 0.5v_o - R_L \tag{5}$$

Based on the following relationships from the previous work [12]

$$\Phi = \frac{v_o}{v_c} \tag{6}$$

$$\Phi = \frac{2\Gamma^*}{C_c} \tag{7}$$

where Γ^* was determined from the section 3.5 above, C_c is the partial pressure of CO_2 at the site of rubisco catalysis and was determined by

$$C_c = C_i - \frac{A}{g_m} \quad (8)$$

where A and C_i were determined from gas exchange measurements and g_m was determined from the section 3.3 above.

Rearranging equations (5) – (7), we can estimate v_o and v_c as

$$v_c = \frac{A+R_L}{1-\Gamma^*/C_c} \quad (9)$$

$$v_o = \frac{v_c-A-R_L}{0.5} \quad (10)$$

Supplementary Method 4. Isotopically non-stationary metabolic flux analysis (INST-MFA) model formulation

Pseudo-steady state metabolism was assumed for INST-MFA because no significant changes in the relative pool sizes of most metabolites was observed throughout the 30 min labeling period at each oxygen condition (Supplementary Figure 7). A network model of central metabolism was constructed using the INCA package (version 1.8) to represent the interactions between the C_3 cycle, photorespiration, starch and sucrose synthesis, the TCA cycle, and amino acid metabolism. The stoichiometry of reactions and atom transitions for each reaction is listed in Supplementary Data 1. The INCA model files (in MATLAB readable format) are included in Supplementary Data 8. Metabolic fluxes were estimated by iteratively minimizing the sum of squared residuals (SSR) between the measured and simulated isotopic labeling patterns and external rate measurements. At each iteration, the network model was used to simulate isotopic labeling kinetics for a given set of fluxes. The fluxes were iteratively adjusted until the local optimum was achieved. The optimization was restarted from 100 random initial values of fluxes to find the global optimum (best-fit solution) (Supplementary Data 4).

The INST-MFA modeling reconciles as well as possible all experimental measurements for each oxygen condition, including the time-course mass isotopologue distribution data, rubisco oxygenation rate (v_o), rubisco carboxylation rate (v_c), starch and sucrose production rates, and output flux ratios of amino acids and sucrose measured in vascular exudate. Due to the technical difficulties of collecting exudates at 2% or 40% oxygen, we used exudates collected at 21% oxygen to constrain the output flux ratios of amino acids and sucrose in all models (Supplementary Table 2). Because the leaf export of amino acids and sucrose were stoichiometrically constrained to each other, the leaf export of glycine or serine was calculated by multiplying the output flux by the ratio of glycine or serine to sucrose.

The labeling data of glycolate, glyoxylate, and glycerate were not included in the INST-MFA modeling for the following reasons: Glycolate and glyoxylate were in low abundance, resulting in relatively large variability in the labeling data (Supplementary Data 2). The labeling of glyoxylate and glycerate was extremely slow, with the average ^{13}C-enrichment reaching only 12% and 16% at 30 min of labeling under high oxygen (Supplementary Figure 5). The lower-than-expected pool size and labeling plateau of glyoxylate was also found in another $^{13}CO_2$ labeling study in Arabidopsis [13]. The slow labeling and large pool size of glycerate indicates the presence of large metabolically inactive pools due to cellular

heterogeneity. To accurately describe the labeling kinetics of metabolites such as glycine, serine, and sugar phosphates, dilution parameters were used in the INCA model to introduce metabolic inactive pools that are not significantly ^{13}C-enriched within the 30 min labeling period (Supplementary Data 1).

To test for the presence of the export of photorespiratory glycine and serine to alternative sinks besides phloem, we removed these two equations (dummyGLY -> outGLY, dummySER -> outSER) from the model. This resulted in slightly increased degrees of freedom (1,714 to 1,716), but worse model fitting for 21% oxygen and 40 % oxygen. The SSR increased from 786 to 882 in the 21% oxygen model and increased from 791 to 1,162 in the 40 % oxygen model. However, the SSR for the 2% oxygen model was not changed when these two reactions were removed, consistent with the very little flux through these export reactions under low photorespiratory conditions. Including the export reactions of photorespiratory glycine and serine to alternative sinks improved the goodness of fit between the flux solution and measured data when modeling photorespiratory scenarios.

Although there is limited evidence for the export of glycerate from the photorespiratory pathway, we included this reaction in the model and added the glycerate labeling data. The addition of the glycerate export reaction only slightly changed the model fitting. The glycine and serine export rates were very close to the values estimated from the original model without the glycerate export reaction. The resulting glycerate and glycine export rate was < 0.1 μmol g^{-1} FW hr^{-1} at all oxygen conditions, while the serine export rate was <0.1 μmol g^{-1} FW hr^{-1} at 2% oxygen, 3.7 μmol g^{-1} FW hr^{-1} at 21% oxygen, and 7.0 μmol g^{-1} FW hr^{-1} at 40% oxygen.

Removing all dilution parameters from the model resulted in worse model fitting but predicted the similar trend of export rates of photorespiratory glycine and serine to alternative sinks besides phloem as compared to the model with dilution parameters (Fig. 1). Without dilution parameters, the glycine export rate was <0.1 μmol g^{-1} FW hr^{-1} at all oxygen conditions; the serine export rate was <0.1 μmol g^{-1} FW hr^{-1} at 2% oxygen, 5.0 μmol g^{-1} FW hr^{-1} at 21% oxygen, and 8.1 μmol g^{-1} FW hr^{-1} at 40% oxygen.

Literature Cited

1 Xu, Y., Fu, X., Sharkey, T. D., Shachar-Hill, Y. & Walker, B. J. The metabolic origins of non-photorespiratory CO_2 release during photosynthesis: A metabolic flux analysis. *Plant Physiol* **186**, 297-314 (2021).

2 Lunn, J. E. *et al.* Sugar-induced increases in trehalose 6-phosphate are correlated with redox activation of ADPglucose pyrophosphorylase and higher rates of starch synthesis in Arabidopsis thaliana. *Biochem J* **397**, 139-148 (2006).

3 Fu, X., Yang, H., Pangestu, F. & Nikolau, B. J. Failure to maintain acetate homeostasis by acetate-activating enzymes impacts plant development. *Plant Physiol* **182**, 1256-1271 (2020).

4 Ubierna, N., Holloway-Phillips, M.-M. & Farquhar, G. D. in *Photosynthesis: Methods and Protocols* (ed Sarah Covshoff) 155-196 (Springer New York, 2018).

5 Evans, J. R. & von Caemmerer, S. Temperature response of carbon isotope discrimination and mesophyll conductance in tobacco. *Plant Cell Environ* **36**, 745-756 (2013).

6 Tazoe, Y., von Caemmerer, S., Estavillo, G. M. & Evans, J. R. Using tunable diode laser spectroscopy to measure carbon isotope discrimination and mesophyll conductance to CO_2 diffusion dynamically at different CO_2 concentrations. *Plant Cell Environ* **34**, 580-591 (2011).

7 Evans, J. R., Sharkey, T. D., Berry, J. A. & Farquhar, G. D. Carbon Isotope Discrimination measured Concurrently with Gas Exchange to Investigate CO_2 Diffusion in Leaves of Higher Plants. *Functional Plant Biology* **13**, 281-292 (1986).

8 Laisk, A. K. Kinetics of photosynthesis and photorespiration of C3 in plants. (1977).

9 Walker, B. J., Skabelund, D. C., Busch, F. A. & Ort, D. R. An improved approach for measuring the impact of multiple CO_2 conductances on the apparent photorespiratory CO_2 compensation point through slope–intercept regression. *Plant Cell Environ* **39**, 1198-1203 (2016).

10 Walker, B. J. & Ort D. R. Improved method for measuring the apparent CO_2 photocompensation point resolves the impact of multiple internal conductances to CO_2 to net gas exchange. *Plant Cell Environ* **38**, 2462-24.47 (2015).

11 von Caemmerer, S., Evans, J. R., Hudson, G. S. & Andrews, T. J. The kinetics of ribulose-1,5-bisphosphate carboxylase/oxygenase in vivo inferred from measurements of photosynthesis in leaves of transgenic tobacco. *Planta* **195**, 88-97 (1994).

12 von Caemmerer, S. Biochemical Models of Leaf Photosynthesis. (CSIRO Publishing, 2000). doi:10.1071/9780643103405.

13. Bergman, M. E. et al. An Arabidopsis GCMS chemical ionization technique to quantify adaptive responses in central metabolism. Plant Physiol. 189, 2072–2090 (2022).